

Review

# A Review of Lithium–Sulfur Batteries Based on Metal–Organic Frameworks: Progress and Prospects

Qiancheng Zhu , Weize Sun, Hua Zhou and Deyu Mao \*

Guangxi Key Laboratory of Automobile Components and Vehicle Technology, School of Mechanical and Automotive Engineering, Guangxi University of Science and Technology, Liuzhou 545006, China; zhuqc@gxust.edu.cn (Q.Z.); 19167041314@163.com (W.S.); zhoub\_610@163.com (H.Z.)

\* Correspondence: 100002073@gxust.edu.cn

**Abstract:** Lithium–sulfur batteries (LSBs) are considered candidates for next-generation energy storage systems due to their high theoretical energy density and low cost. However, their practical applications are constrained by the shuttle effect, lithium dendrites, low conductivity, and volume expansion of sulfur. Metal–organic frameworks (MOFs) have emerged as promising materials for addressing these challenges, owing to their exceptional adsorption and catalysis capabilities, coupled with a readily adjustable form-factor design. This review provides a broader perspective by comprehensively examining the applications of MOFs in LSBs, covering their roles in cathodes, separators, and electrolytes from multiple dimensions, including their reaction mechanisms, the development potential of MOFs as cathode materials, and the positive impacts on LSBs’ performance achieved through the preparation of MOFs and modifications of intermediate, separator, and electrolyte. Finally, we provide perspectives on future development directions in this field.

**Keywords:** metal–organic frameworks; lithium–sulfur batteries; cathode; separator; electrolyte

## 1. Introduction



Academic Editors: Daiwei Wang, Meng Liao and Dino Tonti

Received: 19 January 2025

Revised: 10 February 2025

Accepted: 20 February 2025

Published: 22 February 2025

**Citation:** Zhu, Q.; Sun, W.; Zhou, H.; Mao, D. A Review of Lithium–Sulfur Batteries Based on Metal–Organic Frameworks: Progress and Prospects. *Batteries* **2025**, *11*, 89. <https://doi.org/10.3390/batteries11030089>

**Copyright:** © 2025 by the authors. Licensee MDPI, Basel, Switzerland. This article is an open access article distributed under the terms and conditions of the Creative Commons Attribution (CC BY) license (<https://creativecommons.org/licenses/by/4.0/>).

As economic growth and population expansion persist, global energy consumption and demand are experiencing substantial increases. To mitigate the rapid depletion of fossil fuels and accompanying environmental issues, it is imperative for contemporary society to reduce reliance on fossil energy and expedite the search for viable alternative energy sources [1]. However, lithium-ion batteries fall short of fulfilling the application demands for high specific energy. Consequently, the development of novel energy storage systems possessing high energy densities is of utmost importance. Lithium–sulfur batteries (LSBs) distinguish themselves among various energy storage systems and have recently garnered considerable research attention. This is attributed not only to their theoretically exceptional high energy density ( $2600 \text{ Wh kg}^{-1}$ ) but also to their eco-friendliness and economic viability [2–4]. Furthermore, sulfur is particularly amenable to large-scale production owing to its abundant natural occurrence, ready availability, and non-toxic nature to humans. Consequently, LSBs are widely recognized as a leading candidate for next-generation energy storage solutions due to their significant potential [5].

Through continuous and in-depth research, it has been acknowledged that the cathode of lithium–sulfur batteries (LSBs) poses the primary limiting factor for their development, encompassing issues such as the low conductivity of sulfur, volume expansion, and the shuttle effect [6,7]. Over the years, extensive research has led to the widespread resolution of these challenges through innovative designs of the cathode or separator. Consequently, the capacity and cycle life of LSBs have undergone significant enhancements [8].

In the field of investigating novel materials for electrochemical applications, metal–organic frameworks (MOFs) have emerged as a focal area of extensive research and study [9–11]. The pore structure of MOFs can be tailored by choosing various metal ions and organic ligands. In addition, the unique composition of MOFs endows them with characteristics of both inorganic and organic materials, making them highly promising for advancement in contemporary materials research [12,13]. The highly adjustable pore structure and extremely high specific surface area (SSA) of MOFs make them promising candidates for development in electrochemical studies [14]. It is well established that MOF materials and their derivatives can provide stable pathways for the transport of electrons and lithium ions. They are also effective in mitigating the polysulfide shuttle effect through strong chemical adsorption [15]. Furthermore, their porous structure exhibits robust adsorption capabilities towards lithium polysulfides (LiPSs), thereby effectively mitigating the dissolution of elemental sulfur and polysulfides within organic electrolytes. The one-step carbonization of MOFs offers the advantage of yielding a porous carbon framework and the spontaneous formation of metal nanoparticles, as opposed to the conventional two-step synthesis involving the combination of a metal precursor and carbon source. The utilization of MOFs in electrochemical applications in recent years represents a nascent and rapidly advancing domain [16,17].

At the current stage, there is limited discussion on metal–organic frameworks (MOFs) within the field of lithium–sulfur batteries (LSBs), particularly in regards to their application as cathode materials or separator. This review delves into the reaction mechanisms of lithium–sulfur batteries and explores the potential for their development, highlighting their advantages in terms of energy density, cost-effectiveness, and environmental compatibility. We discuss the preparation methods of MOF materials and the favorable properties that render them suitable for LSB applications. Furthermore, composites consisting of MOFs with graphene, carbon nanotubes (CNTs), and polymers are presented. These composites leverage the combined advantages of MOFs and other materials to further enhance the electrochemical performance of LSBs. Additionally, we present other strategies for improving LSB performance using MOFs, including modifications to the separator and electrolyte with MOF materials. These modification strategies are aimed at mitigating the shuttle effect of polysulfides and improving the cycling stability and safety of the batteries. Our hope is that this contribution will pave the way for future research in the area of MOFs in LSBs.

### 1.1. Overview of Lithium–Sulphur Batteries

The operational principle of lithium–sulfur batteries (LSBs) is rooted in the electrochemical reaction between sulfur and lithium. During the discharge process, sulfur reacts with lithium to produce lithium sulfide ( $\text{Li}_2\text{S}$ ), a reaction that is reversed during charging. Despite the apparent simplicity of this chemical transformation, the practical deployment of LSBs encounters numerous challenges [18]. These include inherent electronic and ionic insulation, the shuttle effect, the growth of lithium dendrites, and the volume expansion of polysulfides, which collectively impair the performance of LSBs. These issues become more pronounced at high sulfur loadings, resulting in rapid capacity degradation [19–21]. Consequently, the development of materials that can facilitate charge transfer, mitigate the shuttle effect, and enhance conversion kinetics is crucial for realizing the practical application of LSBs with high energy densities [22–24].

#### 1.1.1. Reaction Mechanism of Lithium–Sulfur Batteries

In contrast to the typical lithiation/de-lithiation process observed in lithium-ion batteries (LIBs), the sulfur cathode in lithium–sulfur batteries (LSBs) operates through a conversion-type mechanism. This mechanism involves the electrochemical cleavage

and reformation of the S–S bond in  $S_8$ , enabling a complex, multistep, multi-electron, and multiphase redox reaction within LSBs [25–27]. The electrochemical process of multi-electron conversion at the sulfur cathode during both charging and discharging phases is depicted in Figure 1a. During discharge, sulfur undergoes a sequential reduction, initially forming soluble polysulfides ( $Li_2S_8$ ,  $Li_2S_6$ , etc.), which are subsequently converted to sulfur ions in a lower valence state ( $S^{2-}$ ) or persulfide ions ( $S_2^{2-}$ ), ultimately resulting in the formation of solid lithium sulfide. A conventional lithium–sulfur battery (LSB) typically comprises a lithium metal anode, an organic electrolyte, a separator, and a sulfur cathode [28]. The reaction mechanism can be delineated as follows:

1.  $S_8$  to  $Li_2S_8$ : Solid cyclic  $S_8$  is first lithiated to form liquid  $Li_2S_8$  and dissolved in the electrolyte, which is a ‘solid–liquid’ conversion process. This phenomenon aligns with the initial plateau observed in the discharge profile;
2.  $Li_2S_8$  to  $Li_2S_6$ : This stage represents a ‘liquid–liquid’ transformation, taking place at approximately 2.3 V (relative to  $Li^+ / Li$ ), which is associated with the initial plateau in the discharge curve;
3.  $Li^{+}S_6$  to  $Li_2S_4$ : This procedure is depicted by the second gradient. The initial three sulfur transformation steps contribute to approximately 25% of the theoretical discharge capacity, which is around  $419 \text{ mAh g}^{-1}$ ;
4. Conversion of  $Li_2S_4$  to  $Li_2S_2$ : The dissolved ions undergo precipitation to form a solid phase at approximately 2.05 V (relative to  $Li / Li$ ), a process that manifests itself as a second discharge plateau;
5. Conversion of  $Li^{+}S_2$  to  $Li_2S$ : During the discharge process, the accumulation of  $Li_2S_2$  on the electrode surface persists in undergoing reduction to form  $Li_2S$  until the process concludes.

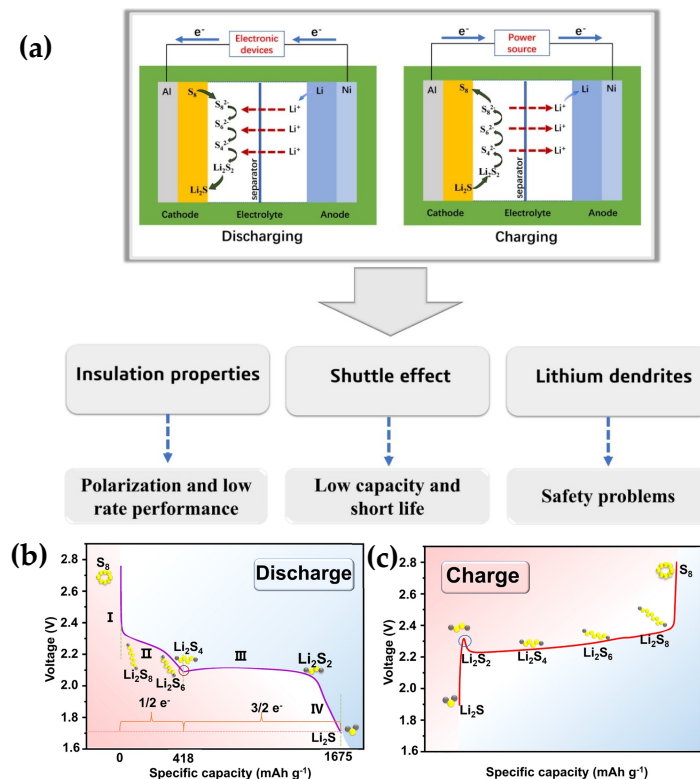


**Figure 1.** (a) LBS reaction mechanism and problems (reprinted/adapted with permission from [28]; copyright 2024, Cell Reports Physical Science). (b) Discharge; and (c) Investigation of charging voltage profiles and associated redox reaction byproducts in LSBs (reprinted/adapted with permission from [29]; copyright 2023, Journal of Energy Chemistry).

Approximately 75% of the theoretical discharge capacity comes from the last two processes, as shown in Figure 1b. The charging process of LSBs is opposite to the discharging process. A typical charging profile is depicted in Figure 1c, illustrating the oxidation of solid  $\text{Li}_2\text{S}$  to form LiPSs, concluding with the regeneration of sulfur. The peak that occurs before the first charging plateau corresponds to the overpotential observed during the oxidation of  $\text{Li}_2\text{S}_2/\text{Li}_2\text{S}$  to LiPSs. This overpotential arises from the difficulty of dissolving solid  $\text{Li}_2\text{S}$ , which has a rather low conductivity of about  $3.6 \times 10^{-7} \text{ S cm}^{-1}$  in LSBs [29].

### 1.1.2. Development Potential of Lithium–Sulphur Batteries

The development potential of LSBs as a new high energy density battery technology is receiving more and more attention. Since the theoretical energy density of LSBs is much higher than that of conventional lithium-ion batteries, this gives them significant potential for use in electric vehicles (EVs) and portable electronic devices [30,31]. Companies such as Oxis Energy and Sion Power, for example, are developing LSBs for the automotive and aerospace industries, aiming to provide longer-lasting, lighter power supplies. Lyten, Inc. of the United States (San Jose, CA, USA) has developed the LytCell lithium–sulfur battery platform, which utilizes 3D graphene materials to significantly increase the energy density of the battery to three times that of conventional lithium-ion batteries. In addition, Lyten has addressed the cycle life of lithium–sulfur batteries through innovative material design. Sulfur is an abundant and low-cost resource, and its cost advantage over the cobalt and nickel used in lithium-ion batteries may lead to more economical energy storage solutions, especially in large-scale applications such as grid storage. The global LSBs market size is estimated at USD 33.8 million in 2023 and is expected to grow at a CAGR of 25.5% from 2024 to 2030. This indicates that the LSBs market is expanding rapidly and is expected to grow significantly in coming years.

Energy densities of 500–600  $\text{Wh kg}^{-1}$  have been achieved in the lab, and commercial products have energy densities around 350–400  $\text{Wh kg}^{-1}$ , such as batteries from OXIS Energy and Sion Power. Companies such as OXIS Energy and Sion Power have launched commercial lithium–sulfur batteries, which are mainly used in drones, aviation, and specialized vehicles, but commercialization still faces challenges such as polysulfide shuttling and a short cycle life. Commercialization still faces challenges such as polysulfide shuttle, lithium dendrite growth, and a short cycle life. In the future, through the optimization of cathode materials, negative electrode protection technology, electrolyte innovation, and battery design improvement, LSBs are expected to achieve large-scale applications in electric vehicles, aviation, and energy storage, and become an important choice for next-generation battery technology.

## 1.2. Metal–Organic Frameworks: Promising Materials for Lithium–Sulfur Batteries Applications

MOFs typically consist of inorganic metal atoms, ions, or metal clusters serving as coordination centers, which interconnect with organic ligands through various coordination modes to yield highly ordered crystalline materials [32,33]. These materials can exhibit extended, periodic structures in one-dimensional (1D), two-dimensional (2D), or three-dimensional (3D) configurations. The pores within MOFs can be classified as microporous (less than 2 nm in diameter), mesoporous (ranging from 2 to 50 nm), or macroporous (greater than 50 nm), with microporous MOFs being the most prevalent. Owing to their distinctive structures and properties, MOFs demonstrate considerable potential for applications across multiple fields and represent an active and significant research direction within materials science.

### 1.2.1. Overview of Metal–Organic Frameworks

As illustrated in Figure 2, the chemical composition, surface area, and pore size of the synthesized MOFs can be precisely controlled through human intervention during the synthesis process [34,35]. Generally, the structure and properties of metal–organic frameworks (MOFs) can be readily tailored by manipulating various synthetic parameters. These parameters encompass the selection of raw materials, such as metal precursors and organic ligands, the synthesis conditions including temperature, pH, and ionic concentration, as well as the employed synthesis methods, such as hydrothermal synthesis or microwave irradiation [36]. Another valuable strategy is post-synthetic modification (PSM), a routine method for functionalizing organic ligands and incorporating secondary metal nodes [37]. The tunable nature of MOFs renders them suitable for integration into supercapacitor applications and rechargeable batteries. Furthermore, the robust framework derived from MOFs can endure the physical stresses associated with the insertion and extraction of metal cations during operation.

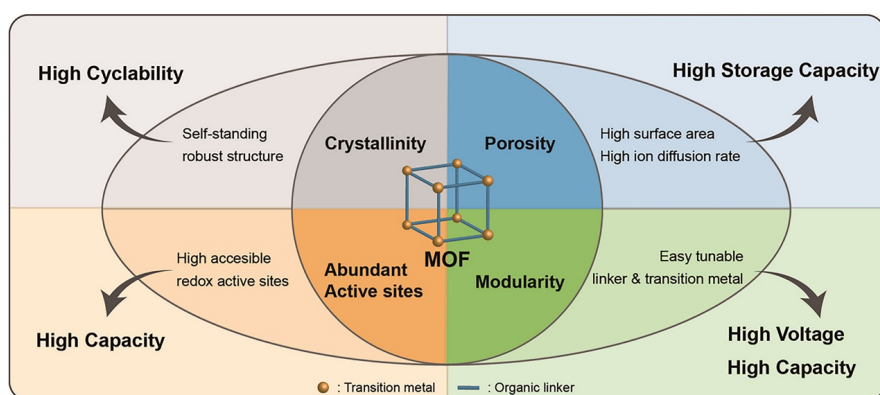


**Figure 2.** Advantages of MOF as a battery cathode material (reprinted/adapted with permission from [38]; copyright 2024, *iScience*).

### 1.2.2. Preparation of Metal–Organic Framework Materials

In recent years, considerable efforts have been dedicated to improving the performance of metal–organic frameworks (MOFs) through their integration with diverse functional materials, including carbon polymers, enzymes, graphene, and metal nanoparticles (NPs). This integration has facilitated the development of composite materials that possess superior properties and exhibit broader application prospects. The resultant MOF composites not only exhibit enhanced intrinsic properties contributed by the individual components but also showcase novel physicochemical properties arising from synergistic effects. The integration of MOFs and functional materials is anticipated to pave the way for advanced energy technologies.

The preparation principles of the aforementioned four metal–organic framework (MOF) composites will be concisely outlined, with Figure 3a–d providing schematic diagrams illustrating the structure of each composite.

1. MOF composites with polymers: Polymers are characterized by their flexibility, strength, and processability, in contrast with the crystalline and rigid nature of MOFs. By combining them, their respective advantages can be preserved. Several methods can be employed to achieve MOF–polymer composites. One approach involves blending MOFs with polymers to create a hybrid matrix film. Another method consists of covalently attaching polymers to the surface of the MOFs [39].
2. MOF and enzyme composite: MOFs serve as carriers for enzyme immobilization, with incorporation methods broadly categorized into the co-precipitation embedding

method and the biomimetic mineralization encapsulation method. In the co-precipitation method, auxiliary stabilizers are utilized to maintain the enzyme's active form during the preparation process, ensuring encapsulation of the enzyme within the MOF structure. Alternatively, biomimetic mineralization, which does not require co-precipitants, involves directly mixing the enzyme with its corresponding MOF to form enzyme-MOF bio-complexes [40]. The key distinction lies in the location of the enzyme: in the former method, it is encapsulated inside the MOF, whereas in the latter, it is associated with the exterior of the MOF.

3. MOF and graphene composites: The preparation of graphene/MOF composites typically involves three methods: in situ growth, interfacial growth, and co-molding. In the in situ growth method, the graphene matrix serves as a template to induce the growth of MOFs on its surface and within its internal pores. Alternatively, the interfacial growth and co-molding methods are employed to form composites by uniformly dispersing MOFs in a graphene solution, either through physical mixing or chemical binding [41].
4. MOFs and metal nanoparticles (NPs): MOFs materials are used as the main materials, and the precursors of metal NPs are confined in the limited space of MOFs materials by the one-pot method, solution impregnation, vapor-phase deposition and solid-state milling, and then the size and morphology of the metal NPs are achieved by adding reductants or energizing the reducing gases, etc. These materials not only inherited the porous nature of MOFs but also combined with the high catalytic activity of metal nanoparticles, which makes the composites exhibit higher efficiency and selectivity in catalytic reactions [42].

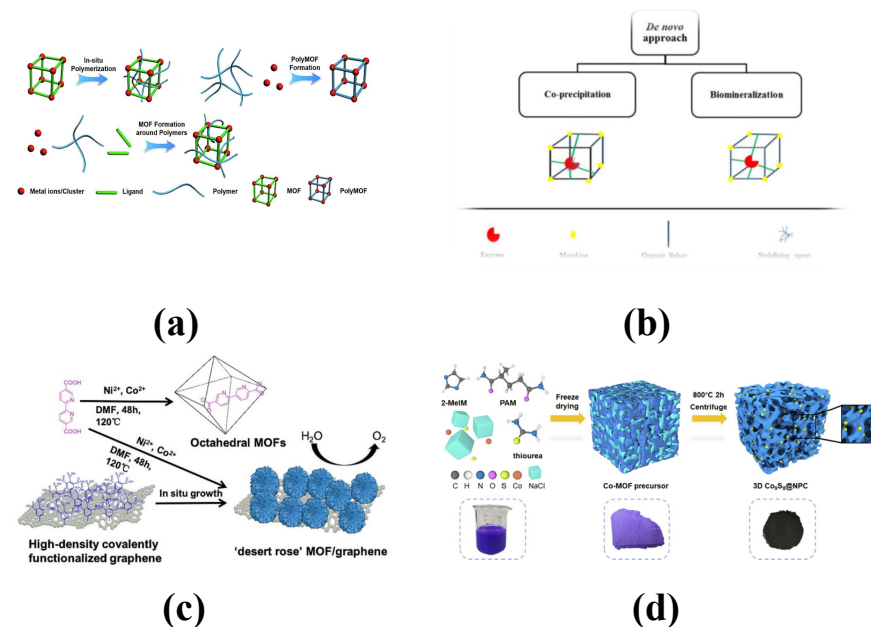


**Figure 3.** (a) MOF complexed with polymer (reprinted/adapted with permission from [39]; copyright 2021, *Coordination Chemistry Reviews*). (b) MOF complexed with enzyme (reprinted/adapted with permission from [40]; copyright 2020, *International Journal of Biological Macromolecules*). (c) MOF complexed with graphene (reprinted/adapted with permission from [41]; copyright 2023, *Journal of Electroanalytical Chemistry*). (d) MOF complexed with metal NPs (reprinted/adapted with permission from [42]; copyright 2022, *Applied Surface Science*).

## 2. Metal–Organic Frameworks for Cathode Applications in Lithium–Sulfur Batteries

MOFs possess a highly ordered porous structure, adjustable pore sizes, and abundant chemical functionalities, rendering them promising candidates as sulfur carriers,

diaphragm modification materials, and electrolyte additives in LSBs. Furthermore, the metal centers and organic ligands within MOFs can serve as catalytic sites, accelerating the conversion of polysulfides. This catalytic effect facilitates the kinetics of the redox reactions in LSBs, ultimately enhancing battery performance. This section delves into five types of MOF-related materials for LSBs applications: pristine MOFs and several distinct types of MOF composites.

### 2.1. Original Metal–Organic Frame

Original MOFs with regularly arranged crystalline structures of inorganic metal and organic components show great potential for storing reactive sulfur in a chain structure prior to discharge, as well as efficiently trapping PSs through chemical affinity and adapting to volume changes during discharge.

The scientific development of MOFs as sulfur hosts in LSBs dates to 2011. Tarascon et al. [43] reported a mesoporous chromium-based MOF, named MIL-100 (Cr) (MIL stands for Matérial Institut Lavoisier), as a host material for sulfur impregnation. Although 48 wt.% sulfur was successfully loaded into the pores of MIL-100 (Cr), which boasts a specific surface area of  $1485 \text{ m}^2 \text{ g}^{-1}$ , the cycling stability of the battery was found to be poor. This was attributed to weak bonding between the polysulfides and the host material, resulting in inefficiencies during the battery's charge–discharge cycles.

Subsequent studies of MOFs primarily concentrated on exploring the impact of MOF pore structure and pore size on their properties. For instance, Hong and co-workers Tang et al. [44] synthesized three flower-like microporous nitrogen-doped carbon nanosheets, designated as FMNCN-n (where  $n = 700, 800$ , and  $900$ , corresponding to the controlled temperature used during synthesis), through the Zn-TDPAT carbonation of metal–organic frameworks (MOFs). As depicted in Figure 4a, these nanosheets exhibited distinct characteristics. The results indicated that FMNCN-900, obtained by carbonizing Zn-TDPAT at  $900^\circ\text{C}$ , possessed an optimal pore volume and nitrogen content. Additionally, Figure 4b revealed a similar pore size distribution across all FMNCN-n compounds. The main pore size of FMNCN-900 is approximately  $0.55 \text{ nm}$ , which falls within the range of  $<0.6 \text{ nm}$ . Notably, the pore size distribution of FMNCN-900 is predominantly centered around  $0.55 \text{ nm}$ . Among the three FMNCN-n materials, FMNCN-900 exhibits the highest pore volume for pore sizes below  $0.6 \text{ nm}$ , making it particularly suitable for accommodating small sulfur molecules. The prepared S@FMNCN-900 cathode material demonstrated exceptional electrochemical performance in lithium–sulfur batteries (LSBs) with carbonate as the electrolyte, as illustrated in Figure 4c. After 200 cycles at a rate of  $0.1 \text{ C}$ , the reversible capacity was approximately  $1220 \text{ mAh g}^{-1}$ . Furthermore, even after 1000 cycles at a higher rate of  $2 \text{ C}$  over an extended period, the reversible capacity remained around  $727 \text{ mAh g}^{-1}$ , with a minimal capacity loss of only about  $0.02\%$  per cycle.

MOFs have been employed as templates for the synthesis of porous carbon materials that are embedded with metal oxides or doped with impurity atoms. These materials offer significant advantages in terms of their catalytic performance and ability to adsorb polysulfides. Jeon et al. [45] developed a core-shell structural template by growing zeolite imidazolate framework-67 (ZIF-67) on ZnO nanorods, as depicted in Figure 5a. This template features a bimetallic Zn/Co-MOF shell surrounding the ZnO core. Upon further carbonization, a hollow carbon composite, designated as Co/Co<sub>3</sub>O<sub>4</sub>-NHC, was obtained. This composite exhibits controllable particle size, a large microporous and mesoporous space, and a strong chemical affinity, making it a promising candidate for applications in lithium-ion batteries. As illustrated in Figure 5b, the adsorption experiment revealed that Co/Co<sub>3</sub>O<sub>4</sub>-NHC exhibits a significantly higher adsorption capacity for lithium polysulfide than the other two materials. After 100 cycles, the battery was disassembled, and a com-

parison of the diaphragms further confirmed that Co/Co<sub>3</sub>O<sub>4</sub>-NHC possessed a markedly stronger adsorption capacity. As shown in Figure 5c, the S@Co/Co<sub>3</sub>O<sub>4</sub>-NHC cathode maintained its morphology well after cycling, indicating that the Co/Co<sub>3</sub>O<sub>4</sub>-NHC composite effectively inhibits the dissolution of lithium polysulfides (LiPSs). In contrast, the initial morphology of the S@NHC cathode underwent significant changes due to its insufficient chemisorption affinity for LiPSs. This resulted in the formation of irregular discharge products covering the surface, which explains its inferior electrochemical performance.

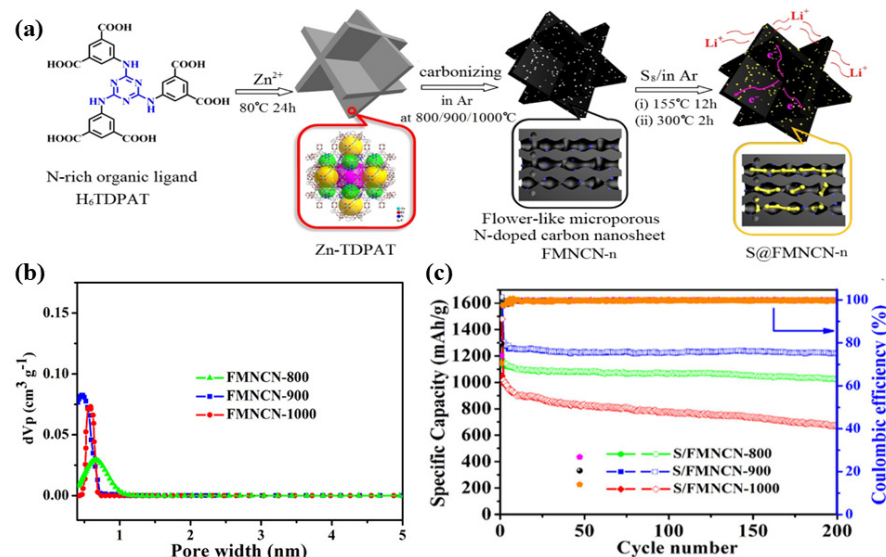


**Figure 4.** (a) Schematic of the preparation of floral Zn-TDPAT, floral microporous nitrogen doped carbon nanosheets (FMNCN-n) and their S/FMNCN-n ( $n = 800, 900$ , and  $1000$ ) composites. (b) Pore size distributions obtained by the NLDFT method using MOF-derived microporous N-doped carbon materials. (c) S/FMNCN-n ( $n = 800, 900$  and  $1000$ ) cathode performance for 200 cycles at  $0.1$  (reprinted/adapted with permission from [44]; copyright 2018, *Applied Materials*).

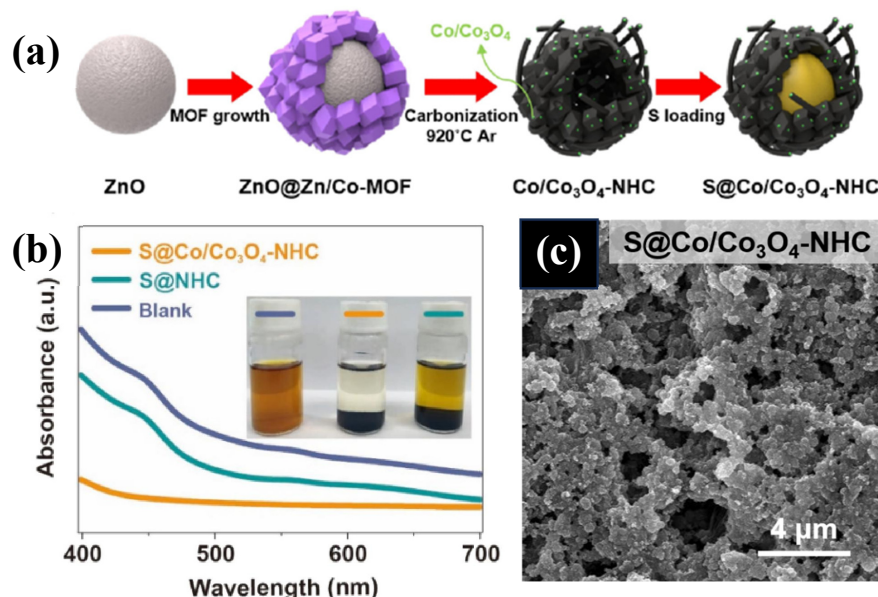


**Figure 5.** (a) Schematic of the synthesis process of S@Co/Co<sub>3</sub>O<sub>4</sub>-NHC. (b) UV-Visible absorption spectra of 10 mM Li<sub>2</sub>S<sub>6</sub> solution containing Co/Co<sub>3</sub>O<sub>4</sub>-NHC, NHC and Co-NC. The inset shows a photograph of Li<sub>2</sub>S<sub>6</sub> solution after stirring for 24 h. (c) SEM image of S@Co/Co<sub>3</sub>O<sub>4</sub>-NHC cathode after 100 cycles (reprinted/adapted with permission from [45]; copyright 2021, *Chemical Engineering Journal*).

## 2.2. Metal–Organic Framework Composites

Recent advancements are being achieved in the technology pertaining to the utilization of MOF composites in LSBs, especially in improving the multiplicity performance, cycle stability and energy density of the cells. The latest technological advancements encompass the structural optimization, functionalization, and integration of MOFs with other materials to facilitate more efficient sulfur utilization and polysulfide immobilization. The composite formation of MOFs with graphene, carbon nanotubes, and other conductive materials establishes an effective electron transport network, which substantially augments the conductivity of the sulfur cathode and elevates the multi-faceted performance of the battery. Furthermore, the metal nodes within the MOFs can function as catalytic centers, facilitating the polysulfide conversion reaction and subsequently enhancing the charging and discharging efficiency of the battery.

### 2.2.1. Composites with Graphene

The pioneering utilization of graphene as a cathode material for LSBs was reported by Park and Yu et al. [46], who synthesized sulfur particles within the interlayer spaces of graphene sheets to serve as the cathode in LSBs. Graphene is renowned for its exceptional conductivity and charge carrier mobility, substantial specific surface area, outstanding transparency, remarkable flexibility, and high mechanical strength across various applications. These attributes render graphene a suitable candidate for enhancing the conductivity of electrodes [47]. Hence, the combination of MOFs with graphene in hybrid structures allows for capitalization on their unique strengths, resulting in the manifestation of synergistic effects.

For instance, Baumann and co-workers [48] designed a high-density nanocomposite electrode with minimal carbon content by integrating Zr-based MOF-808 (employing sulfur as the active component) with a graphene/ethyl cellulose additive. In contrast to conventionally employed carbon/binder blends, these nanocomposite materials exhibit enhanced specific capacity and a more compact structure. The sulfur-laden MOF and graphene nanosheet composites are designated as MOF-808@S/GE'. As illustrated in Figure 6a, MOF-808@S/GEC demonstrates a more compact structure than the other materials. Furthermore, Jiao et al. [49] fabricated a three-dimensional composite consisting of an indium metal–organic framework integrated with reduced graphene oxide (In-IPA@rGO) as a sulfur host for LSB applications using a straightforward two-step hydrothermal method, as depicted in Figure 6b. The In-IPA@rGO composite boasts a three-dimensional hierarchical structure and abundant catalytically active sites, which are favorable for mitigating polysulfide volume expansion and the shuttle effect. The SEM images of In-IPA@rGO and the EDS analysis of In-IPA@rGO/S in Figure 6c,d clearly reveal the material's three-dimensional structure. The In-IPA@rGO/S cathode exhibited an initial discharge capacity of  $1672.3 \text{ mAh g}^{-1}$ , and the capacity was maintained at  $898.7 \text{ mAh g}^{-1}$  with a Coulombic efficiency (CE) close to 100% after 100 cycles at 0.2 C. However, the initial discharge capacity of the In-IPA/S cathode was  $1099.4 \text{ mAh g}^{-1}$ , which decreased dramatically to  $296.7 \text{ mAh g}^{-1}$  after 100 cycles. From these results, it can be seen that the battery performance of In-IPA@rGO composites is improved, which may be due to the synergistic effect between In-IPA and rGO.

### 2.2.2. Composites with Carbon Nanotubes (CNTs)

In contrast to graphene, carbon nanotubes (CNTs) exhibit one-dimensional tubular structures, yet their structural versatility enables researchers to customize them according to specific requirements [50,51]. Xu et al. [52] synthesized metal–organic framework-74-Ni/carbon nanotube (MOF-74-Ni/CNT) composites by an *in situ* hydrothermal reaction in a one-pot method form; see Figure 7a. This distinctive architecture not only offers a high density of open metal sites to anchor polysulfides but also ensures extended electrical

contacts. What is particularly novel is that Zhou et al. [53] exploited the different thermal stabilities between ZIF-67 and ZIF-8 to synthesize carbon nanotubes (CNTs) grafted onto nitrogen-doped carbon@graphitic carbon nanocages (CNT-NC@GC) through the pyrolysis of the core-shell structured ZIF-8@ZIF-67. The design incorporates several structural merits. The carbon shell, characterized by high porosity and a high specific surface area, not only offers ample space for loading high quantities of sulfur but also significantly diminishes ion/electron transfer pathways. Consequently, the CNT-NC@GC/S composite, with a sulfur content nearing 80%, experiences enhanced utilization of the active material [54]. Figure 7b illustrates the formation process of the CNT-NC@GC/S cathode material. Additionally, Figure 7c presents the TEM image along with the corresponding elemental mapping of ZIF-8@ZIF-67, comprising a ZIF-8 core encapsulated within a ZIF-67 shell. Based on the most recent experiments, Wang et al. [55] synthesized the reactive material CoMoS<sub>3.13</sub>@NCNTs by initially coating an MOF material onto metal oxides as a precursor. This precursor was subsequently treated with sulfide to ultimately yield a composite rod-layer structure of the active material, as depicted in Figure 7d. During the synthesis process, the MoO<sub>3</sub>@ZIF-67 precursor formed nanorod-like structures with numerous voids through ion exchange with S<sup>2-</sup> ions and mutual ion exchange between Mo ions in MoO<sub>3</sub> nanorods and Co ions in ZIF-67. Figure 7e demonstrates that after 400 cycles, the CoMoS<sub>3.13</sub>@NCNTs maintain a discharge capacity of 785 mAh g<sup>-1</sup> with a Coulombic efficiency of 97%. In comparison, they exhibit an advantage over CoMoS<sub>3.13</sub>. Hence, due to their excellent electrical conductivity and high specific surface area, CNTs have been widely employed to boost the rate capability and elevate the sulfur content in MOF-based composite materials.

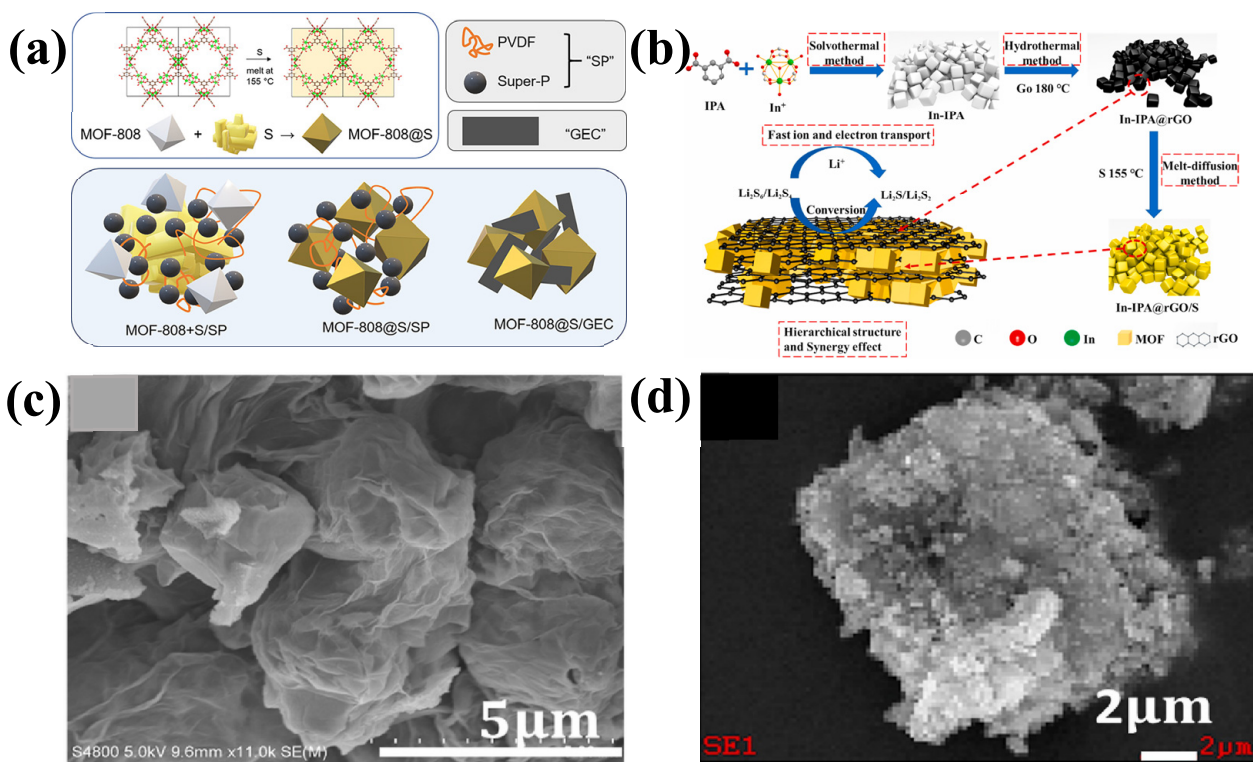


**Figure 6.** (a) Graphical representation of the sulfur loading procedure in a representative MOF-808 (top panel) and cartoon representations of different electrode compositions highlighting the bulk densities provided by the various components (bottom panel) (reprinted/adapted with permission from [48]; copyright 2020, *Applied Materials*). (b) Schematic representation of the synthesis of In-IPA@rGO/S composites. (c) SEM image of In-IPA@rGO. (d) EDS mapping of In-IPA@rGO/S (reprinted/adapted with permission from [49]; copyright 2022, *Ceramics International*).

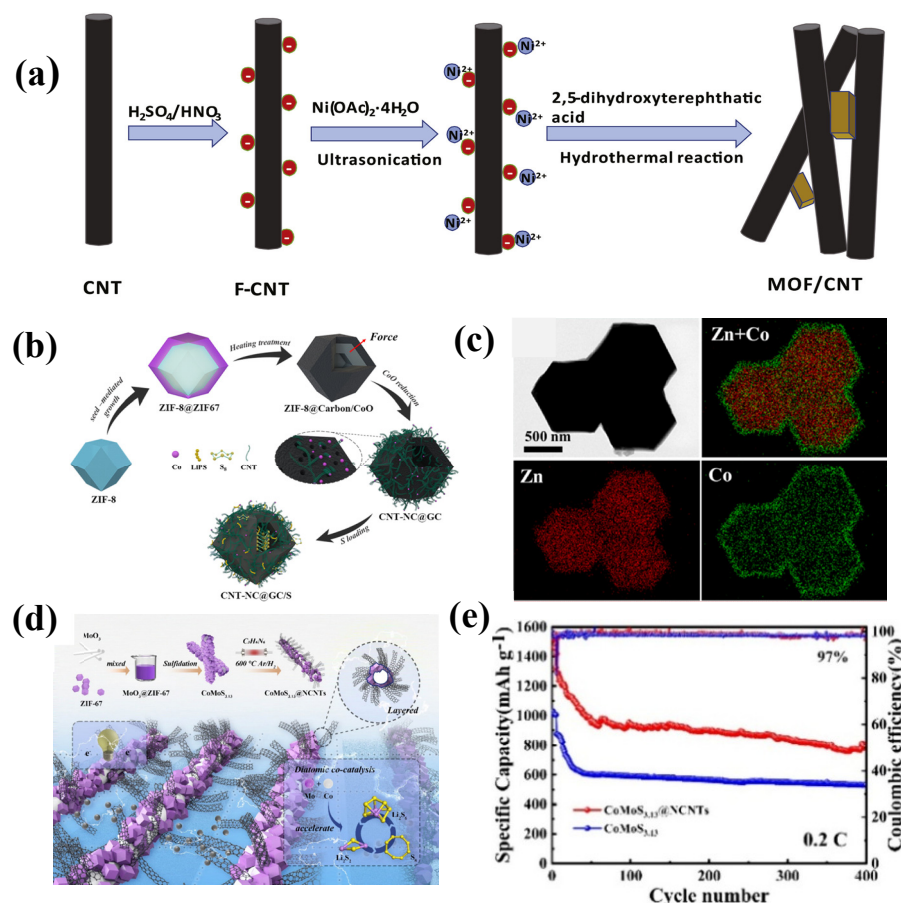


**Figure 7.** (a) Schematic of the synthesis of MOF-74-Ni/CNT (reprinted/adapted with permission from [52]; copyright 2018, *Journal of Electroanalytical Chemistry*). (b) Diagram of the formation process of CNT-NC@GC/S cathode material. (c) TEM image of precursor ZIF-8@ZIF-67 and corresponding elemental mapping (reprinted/adapted with permission from [53]; copyright 2020, *Electrochimica Acta*). (d) Schematic of the synthesis of CoMoS<sub>3.13</sub>@NCNTs composite. (e) Cycling diagram of CoMoS<sub>3.13</sub>@NCNTs at 0.2 C Cycle diagram of CoMoS<sub>3.13</sub>@NCNTs with CoMoS<sub>3.13</sub> (reprinted/adapted with permission from [55]; copyright 2024, *ACS Sustainable Chemistry & Engineering*).

### 2.2.3. Composites with Conductive Polymers

The integration of conducting polymers with MOFs represents an alternative efficient strategy for constructing intricate structures aimed at enhancing the performance characteristics of MOF-based cathode materials. On one hand, conducting polymers substantially bolster the inherently low conductivity of sulfur-based cathodes and expedite electron transport, thereby further elevating the electrochemical performance. On the other hand, these polymers harbor polar bonds, including C-H and N-H, which facilitate chemical anchoring of polysulfides (PSs) and effectively mitigate the shuttling effect [55]. Notably, among the variety of conductive polymers, polypyrrole (PPY) and polyaniline (PANI) [56,57] exhibit exceptional electrical conductivity. The incorporation of MOFs into cathode materials significantly amplifies the electrochemical performance of LSBs [58].

Liu et al. [59] added polyaniline to the precursor of ZIF-67 by an *in situ* growth technique in the preparation of capacitors, which allowed the nucleation process of ZIF-67 to take place *in situ* under a PANI coating (Figure 8a). Since the fixed central Co(II) ions are electrically neutral and consequently unable to support the free flow of charged electrons, the incorporation of PANI (polyaniline), which boasts exceptional conductivity, ductility, and capacitance, becomes pivotal. The *in situ* growth of PANI within the ZIF-67 framework enables electrons to traverse the composite structure efficiently. This integration

not only substantially boosts the specific capacity but also enhances cycling stability, thereby contributing significantly to the advancement of anode materials for LSBs. As depicted in Figure 8b, the composite cathode demonstrates an initial discharge-specific capacity of  $1220.1 \text{ mAh g}^{-1}$  at a current density of  $0.1 \text{ C}$ , and maintains a reversible capacity of  $1018.7 \text{ mAh g}^{-1}$  after 100 cycles, with a capacity retention rate of 83.5%. Zhang et al. [60] also employed a composite of PANI with MOFs, utilizing hydrochloric acid etching on ZIF-67 followed by high-temperature activation to obtain nitrogen-doped carbon (NC). Subsequently, three-dimensional crosslinked PANI fibers/NC (3CPC) were synthesized through in situ polymerization of aniline (Figure 8c). This 3D interwoven framework is characterized by a high density of micropores and mesopores, which effectively promote sulfur immobilization and enhance ion diffusion. Beyond the physical confinement of LiPSs by the NC framework, the nitrogen-containing functional groups and  $\pi$ -conjugated systems on the PANI framework can serve as active sites or groups to chemically immobilize polysulfides, thereby suppressing the shuttle effect.

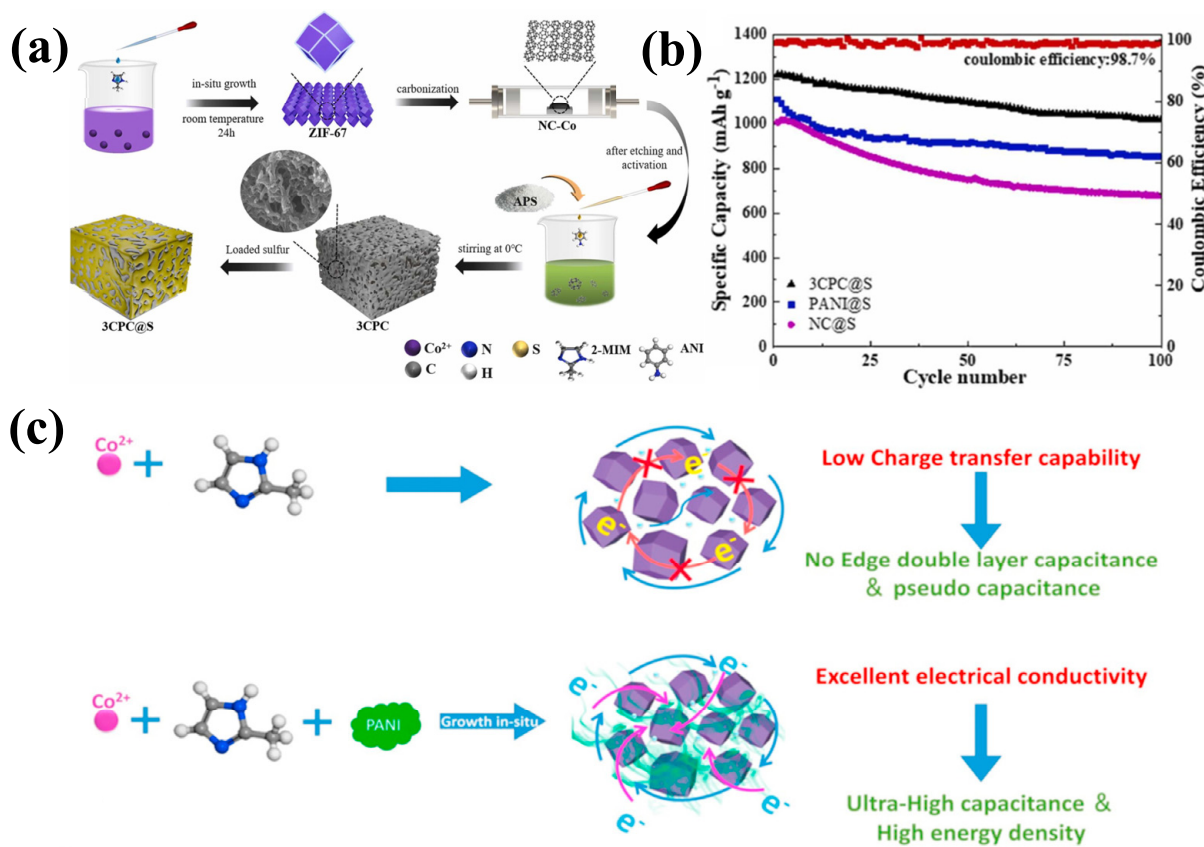


**Figure 8.** (a) Illustration for the preparation processes of 3CPC@S composites. (b) Initial discharge/charging curves of 3CPC@S, PANI@S, and NC@S cathodes at  $0.1 \text{ C}$  (reprinted/adapted with permission from [59]; copyright 2023, *Colloids and Surfaces A: Physicochemical and Engineering Aspects*). (c) Schematic of the fabrication of ZIF-67 and ZIF-67@PANI (reprinted/adapted with permission from [60]; copyright 2021, *Journal of Alloys and Compounds*).

#### 2.2.4. Derivatives of Metal–Organic Frameworks

The utilization of MOF-derived composite materials in LSBs represents an emerging and dynamic research area. These materials can undergo transformations into nanostructured composites comprising porous carbon and metal/metal compounds via methodologies encompassing carbonization, pyrolytic acid treatment, and osmotic dehydration [61,62]. These MOF derivatives maintain their porous structure, exhibiting superior electrical conductivity and a wealth of polar or catalytic sites [63], which can substantially decrease

electrochemical polarization and enhance the redox kinetics in LSBs [64]. Yang et al. [65] designed a bi-directional catalyst based on In-MOF by adjusting the phases of MOF derivatives at different carbonation temperatures, as shown in Figure 9a. As a result,  $\text{In}_2\text{O}_3@\text{C}$  obtained at 400 °C promotes the conversion of  $\text{S}_8$  to soluble long-chain  $\text{Li}_2\text{S}_n$  ( $4 \leq n \leq 8$ ), while  $\text{In}@\text{C}$  obtained at 1000 °C shows excellent catalytic performance in promoting the conversion of  $\text{Li}_2\text{S}_4$  to  $\text{Li}_2\text{S}$  and the dissolution of  $\text{Li}_2\text{S}$ .  $\text{In}-\text{In}_2\text{O}_3@\text{C}$  prepared at 800 °C combines the advantages of the above two derivatives and can catalyze the conversion of lithium-ion batteries in both directions. In Figure 9b, it can be clearly observed that the exchange current density ( $I_0$ ) of  $\text{In}-\text{In}_2\text{O}_3@\text{C}$  is much higher than that of  $\text{In}@\text{C}$  and  $\text{In}_2\text{O}_3@\text{C}$  during the conversion of LiPSs, which suggests that  $\text{In}-\text{In}_2\text{O}_3@\text{C}$  is more conducive to accelerating the kinetics of the redox reaction of LiPSs. The carbonization of bimetallic MOFs can lead to the formation of bimetallic nanoparticles, offering unique advantages that are unattainable with monometallic materials; Meanwhile, carbonization of nanofibers can result in the formation of unique, self-standing carbon nanofiber structures [66]. Wang et al. [67] innovatively synthesized a composite material comprising nitrogen-doped carbon nanofibers loaded with MOF-derived NiCo bimetallic nanoparticles, designated as NiCo-PCNF [68–70]. This synthesis was achieved through a combination of advanced techniques: high-pressure electrospinning, in situ growth, and high-temperature pyrolysis, as illustrated in Figure 9c. The nickel–cobalt bimetallic nanoparticles derived from MOF can be clearly observed in Figure 9d, and the nickel–cobalt metal nanoparticles marked by red circles have a size of 20~40 nm attached to the surface and inner diameter of the carbon nanofibers. According to Figure 9e, the performance shows that the initial specific discharge capacity of the S/NiCo-PCNF cathode is 849.3  $\text{mAh g}^{-1}$ , which is higher than the 836.9, 620.6, and 742.2  $\text{mAh g}^{-1}$  of S/Ni-PCNF, S/Co-PCNF, and S/PCNF. After 500 cycles, the Coulombic efficiency of the S/NiCo-PCNF cathode electrode reached 97.7%, with a decay rate of only 0.099% per cycle. This result further demonstrates the superior co-catalytic electrocatalytic ability of nickel–cobalt bimetallic nanoparticles in the overall sulfur reduction reaction (SRR), which effectively improves the kinetics of the redox reaction of LiPSs, utilizes the reactive species more fully, and exhibits excellent electrochemical cycling performance.

High entropy oxides (HEOs) represent a novel category of crystalline solid solutions, distinct from conventional derivatives, offering a unique combination of randomly dispersed active metal sites, superior electronic conductivity, and synergistic multicomponent interactions that effectively anchor polysulfides. Hassan Raza et al. [71] prepared high entropy oxide ( $\text{Ni}_{0.2}\text{Co}_{0.2}\text{Cu}_{0.2}\text{Mg}_{0.2}\text{Zn}_{0.2}$ ) O (HEO850) from self-sacrificial multi-metal organic frameworks (M-MOFs) via a novel low temperature templating strategy. The battery has an initial specific discharge capacity of 1244  $\text{mAh g}^{-1}$  at 0.5 C and maintains a capacity of 784  $\text{mAh g}^{-1}$  even after 800 redox cycles, with a decay rate as low as 0.043% per cycle. Hassan Raza et al. [72] prepared titanium-containing high entropy oxides (Ti-HEO) with enhanced electrical conductivity in the following year by employing the same facile synthesis technique as low temperature calcination of metal–organic framework (MOF) templates. The Ti-HEO/S/KB cathode demonstrates superior performance compared to the HEO850/S/KB, particularly under high sulfur loading conditions, owing to its enhanced catalytic activity for lithium polysulfide (LPS) conversion and improved electrical conductivity. Typically, it has an initial discharge capacity of up to about 1246  $\text{mAh g}^{-1}$  at a sulfur loading of about 3.4  $\text{mg cm}^{-2}$ , and after 1000 cycles at 0.5 C, the capacity is maintained at about 542  $\text{mAh g}^{-1}$ , with a capacity decay rate of only 0.056% per cycle.

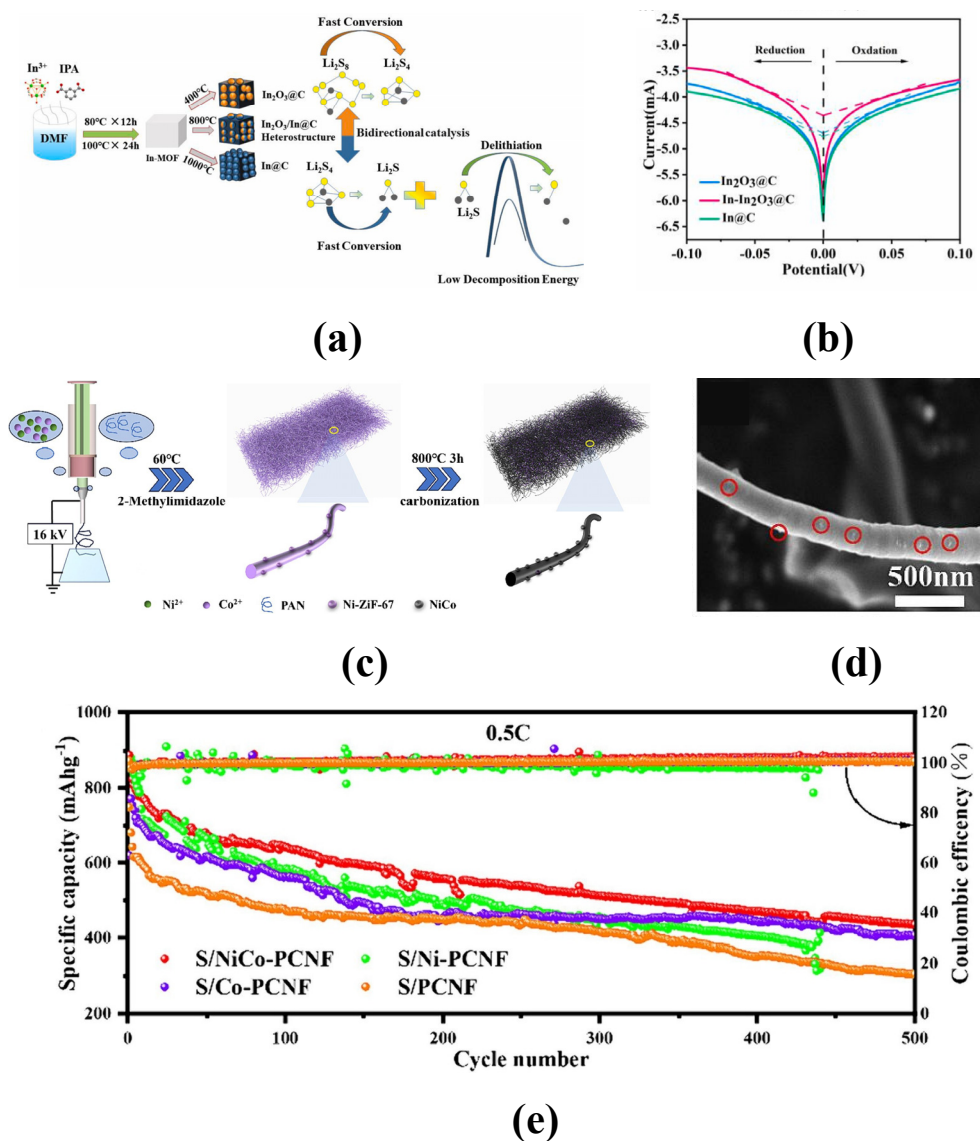


**Figure 9.** (a) Schematic preparation of  $\text{In}_2\text{O}_3@\text{C}$ ,  $\text{In}-\text{In}_2\text{O}_3@\text{C}$ , and  $\text{In}@\text{C}$  composites. (b) Tafel curves of  $\text{In}_2\text{O}_3@\text{C}$ ,  $\text{In}-\text{In}_2\text{O}_3@\text{C}$ , and  $\text{In}@\text{C}$  symmetric cells (reprinted/adapted with permission from [65]; copyright 2024, *Ceramics International*). (c) Schematic of the preparation process of NiCo-PCNF. (d) SEM morphology of NiCo-PCNF. (e) Cycling performances of S/NiCo PCNF, S/Ni-PCNF, S/Ni-PCNF, S/PCNF, and S/PCNF at 0.5 C. (d) SEM morphology image of NiCo-PCNF. (e) Cycling performances of S/NiCoMOF (reprinted/adapted with permission from [67]; copyright 2024, *Journal of Electroanalytical Chemistry*).

The MOF derivatives exhibit robust adsorption and catalytic capabilities towards polysulfides, facilitating rapid catalytic conversion of these species and significantly enhancing the cycling stability and capacity retention of lithium–sulfur batteries. While the material demonstrates a certain level of reversible capacity, substantial efforts are still required to further elevate its performance, particularly in terms of capacity and cycle stability, relative to the anode.

### 3. Alternative Strategies for Metal–Organic Frameworks to Improve the Performance of LSBs

The incorporation of a catalyst material into the sulfur cathode can effectively curb sulfur expansion and hinder the dissolution of soluble polysulfides. However, this incorporation inevitably results in a decrement in the cathode's active material loading. The

utilization of MOFs transcends the confines of the cathode in LSBs, extending to their application within interlayers, separators, and electrolytes as well. In contrast to conventional lithium batteries and other lithium–metal batteries systems, the impact of the intermediate layer in LSBs on performance is significantly more pronounced due to the presence of soluble polysulfides. Given the high porosity, chemical absorption capabilities, and catalytic properties of MOFs, the MOF-modified interlayer can effectively hinder the diffusion of polysulfides towards the counter electrode, thereby mitigating the polysulfide shuttle effect. Theoretically, MOFs with ordered porous channels possess the capacity to accommodate a diverse range of liquid species and achieve the desired molecular/ion sieving/transport effects. Consequently, diaphragms modified with MOFs can facilitate ordered ion transport, promoting uniform lithium deposition [73]. Furthermore, the MOF-modified electrolyte inhibits polysulfide shuttling through potent electrostatic repulsion while providing abundant pathways for rapid lithium-ion transport and safeguarding the lithium anode. These attributes collectively contribute to enhancing the cycling stability and capacity retention of the battery.

### 3.1. Intermediate Layer Modified by Metal–Organic Framework Material

In LSBs, the shuttle effect of soluble intermediate lithium polysulfides (LiPSs) within sulfur cathodes results in the irreversible loss of active material and degradation of the lithium anode, ultimately leading to decreased specific capacity and impaired cycling stability [74]. The insertion of a functional interlayer between the sulfur cathode and separator serves as an effective strategy to inhibit the shuttling of LiPSs, offering advantages such as ease of handling, a broad selection of materials, and multifunctional integration [75]. Non-carbon materials, including layered double hydroxides (LDHs), metal–organic frameworks (MOFs), and metal oxides/sulfides/carbides [76], typically exhibit stronger interactions with LiPSs, rendering them increasingly appealing as interlayer materials for LSBs due to their potential to mitigate the shuttle effect. Yang et al. [77] successfully synthesized heterostructure LDH-MOF (Figure 10a) via a simple solvothermal reaction between NiCo-LDH and 1,4-benzenedicarboxylic acid (BDC). Hybridization of MOFs and LDHs can combine their advantages and is suitable for use as interlayer materials for LSBs. In investigating the electrochemical performance of lithium sulfur batteries (LSBs) utilizing various separators, as illustrated in Figure 10b,c, the Tafel slopes associated with peaks b and c in the cell employing NiCo-MOF/LDH@PE are  $28\text{ mV dec}^{-1}$  and  $69.1\text{ mV dec}^{-1}$ , respectively. These values are significantly smaller than those observed in cells using pure PE, NiCo-LDH@PE, and NiCo-MOF@PE separators. This comparison highlights the remarkable electrocatalytic activity of NiCo-MOF/LDH in enhancing the conversion reactions within lithium-ion batteries. Additionally, Kang et al. [78] synthesized Mg-MOF-74 directly on free-standing carbon paper (MOF/C-paper). By subjecting Mg-MOF-74 to pyrolysis, it was converted into a highly porous carbon material ( $\text{MgO}@C/C$ -paper) with uniformly dispersed magnesium oxide nanoparticles. This composite was then utilized as an interlayer in an LSBs, as depicted in Figure 10d. Three types of LSB coin cells were assembled, each with a cathode sulfur content of  $1.7\text{ mg cm}^{-2}$ . These included a standard cell without any interlayer, a cell with a C-paper interlayer positioned between the cathode and the separator, and a cell with an  $\text{MgO}@C/C$ -paper interlayer sandwiched between the cathode and the separator. The cyclic tests shown in Figure 10e were performed at a current density of  $0.2\text{ C}$  with cut-off voltages of 1.7 and 2.8 V. The cyclic tests were performed at a current density of  $0.2\text{ C}$  with a cut-off voltage of 1.7 and 2.8 V. In addition, the Coulomb efficiencies after 200 cycles were 98.3%, 98.7% and 99.0% for standard, C and  $\text{MgO}@C/C$  papers, respectively. The high electrical conductivity and large surface of the interlayer provide many reaction sites for polysulfides and improve polysulfide utilization. However, the formation of  $\text{Li}_2\text{S}_2$  and

$\text{Li}_2\text{S}$  is expected to eventually passivate the surface of the C paper, while the  $\text{MgO}@\text{C}$  layer prevents passivation.

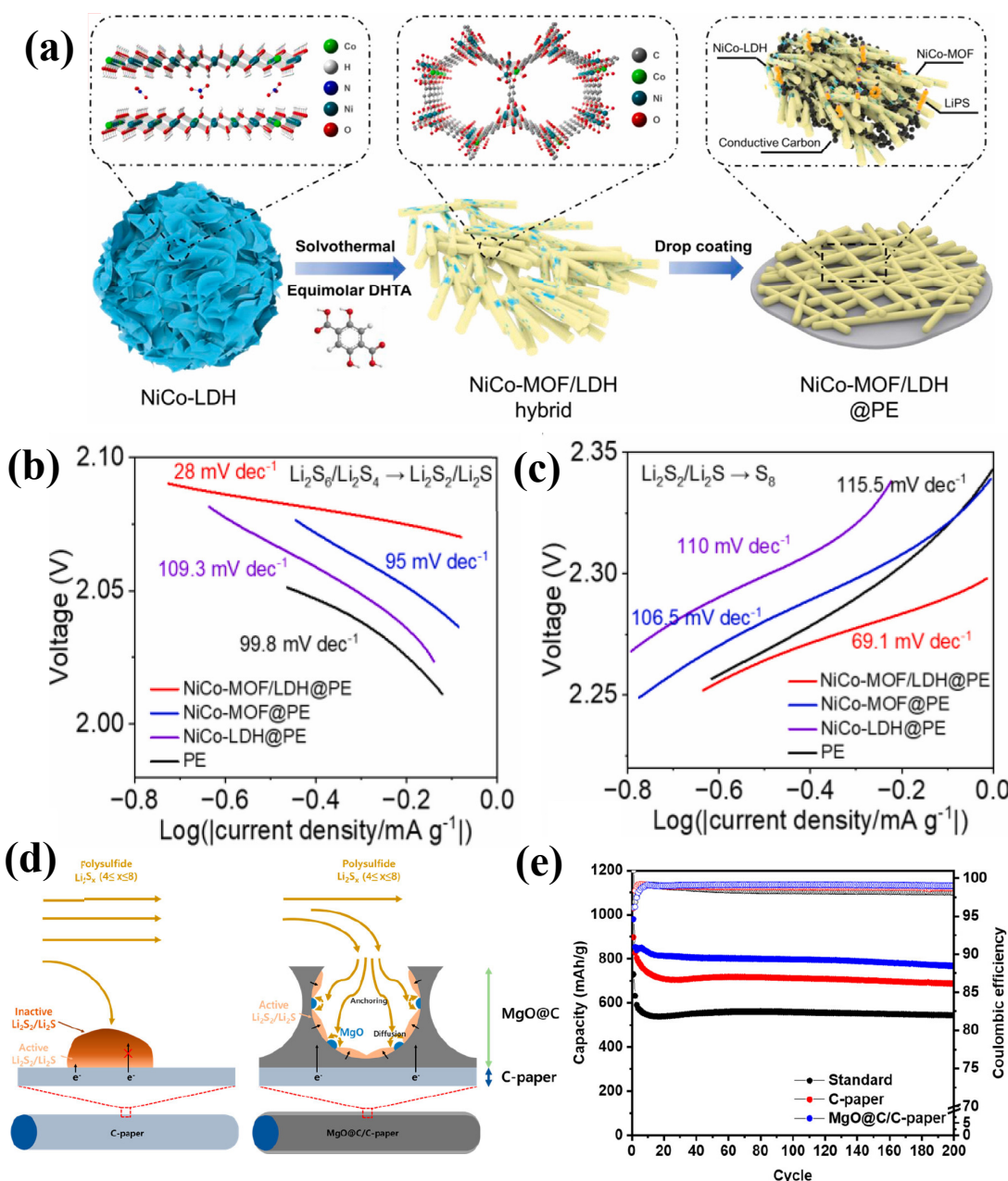


**Figure 10.** (a) Schematic representation of the transition from layered NiCo-LDH to NiCo-MOF/LDH nanorods and the subsequent preparation of NiCo-MOF/LDH@PE. (b,c) Tafel plots of peaks b (b) and c (c) (reprinted/adapted with permission from [77]; copyright 2023, *Materials Today Physics*). (d) Schematic representation of the redox reaction of polysulfides on C and MgO@C/C papers; MgO nanoparticles anchor the dissolved polysulfides and diffuse onto the carbon composites for reduction. (e) Reduction of polysulfides without an interlayer (labelled ‘standard’), C paper, and MgO@C/C paper at 0.2 °C sulfide, and diffuses onto the carbon composite for reduction. (e) Electrochemical performance of lithium–sulfur batteries without interlayer (labelled ‘standard’), C paper, and MgO@C/C paper interlayer at 0.2 °C. Cycling performance with sulfur loading mass of 11.7 mg cm<sup>-2</sup> charge-discharge curves (reprinted/adapted with permission from [78]; copyright 2023, *ACS Sustainable Chemistry & Engineering*).

### 3.2. Separators Modified by Metal–Organic Framework Materials

The dissolution of polysulfides and resulting shuttle effects are the primary obstacles hindering the long-term cycle life and capacity retention of LSBs. To address these challenges, Razaq et al. [79] used a one-step solid solution phase synthesis method to design efficient separators that were modified with bifunctional bimetallic MOFs (Figure 11a). Figure 11b clearly shows by CV redox peaks that the cathodic peak intensity of Fe-ZIF-8/PP increases and anodic peak decreases as compared to ZIF-8/PP and PP, which suggests the effective conversion of polysulfides by Fe-ZIF-8/PP. LSBs with PP and ZIF-8/PP, Fe-ZIF-8/PP separators, S-CNT/GO anodes, and Li-negative electrodes were assembled into 2032-type coin cells and their long-term cycling performance was evaluated. As shown in Figure 11c, the discharge capacity of Fe-ZIF-8/PP is  $865 \text{ mAh g}^{-1}$ , and the capacity after 1000 cycles is  $409 \text{ mAh g}^{-1}$ , with a Coulombic efficiency of  $\approx 100\%$  at 0.5 C. The layers modified using current techniques exhibit gaps between the MOFs that are considerably larger than the MOFs' inherent pore size. Polysulfides and lithium ions inevitably pass through these gaps, hindering the full utilization of the structural benefits. Zhou and Dong et al. [80] formed ultra-thin (20 nm) and crack-free MOF films on the diaphragm by atomic layer deposition (ALD) (Figure 11d). The confinement of polysulfides by ZIF-8 films was observed by the simplest visual experiment, as shown in Figure 11e for the permeation test of a double L device separated by F/ZIF-PP, G-PP diaphragm. The device with G-PP separator showed no significant penetration of polysulfides at the beginning due to the physical blockage of the ZIF particle layer. After 12 h, the electrolyte on the right side of the device began to turn yellow and progressively darkened, indicating that the polysulfide shuttle effect was gradually intensifying. For the unit with the F/ZIF-PP separator, there was almost no penetration of polysulfides even after 48 h, and by comparing the F/ZIF-PP showed good performance. Functional coatings on separators not only play a crucial role in regulating pore size, interfacial properties, wettability, porosity and the internal structure of the membrane but they are also a key factor in the development of the membrane [81,82]. It also enhances the membrane's ion transport capability and regulates lithium polysulfide intermediates via both physical and chemical constraints, providing sufficient active sites for the anchoring and conversion of lithium polysulfide intermediates [83–86]. Zhao et al. [87] prepared a new separator based on a coating design, where Zn-MOF was synthesized and then Y-MOF was grown on its surface. Subsequently,  $\text{Y}_2\text{O}_3/\text{ZnO}@\text{C}$  composites were synthesized by high-temperature calcination, which were finally coated on polyethylene separators. Figure 11f displays a TEM image of  $\text{ZnO}@\text{C}$ , revealing its distinctive rod-like structure. Upon revisiting Figure 11g, we observe a TEM image of  $\text{Y}_2\text{O}_3/\text{ZnO}@\text{C}$ , where smaller  $\text{Y}_2\text{O}_3@\text{C}$  particles are visibly growing on the surface of the  $\text{ZnO}@\text{C}$  rods. To evaluate the electrochemical performance of the modified separators,  $\text{Y}_2\text{O}_3/\text{ZnO}@\text{C}$ ,  $\text{ZnO}@\text{C}$ , and  $\text{Y}_2\text{O}_3@\text{C}$  were used on one side of the separator, followed by the assembly of the cells and long-term cycling tests. Figure 11h presents the charge–discharge profiles of various separators at a rate of 0.5 C. It is evident that  $\text{Y}_2\text{O}_3/\text{ZnO}@\text{C}$  shows a stable plateau and achieves the highest specific charge–discharge capacity.

### 3.3. Electrolytes Modified by Metal–Organic Framework Materials

The degradation of lithium anodes in LSBs poses a significant threat to their safety and recyclability. The uneven distribution of lithium during repeated plating/stripping processes leads to the formation of ‘dead lithium’ and subsequent capacity loss. Furthermore, it destabilizes the solid electrolyte interphase (SEI) layer, as reported in studies [88,89]. In conventional LSBs, the lithium anode operates in a highly complex environment, where insoluble  $\text{Li}_2\text{S}$  and  $\text{Li}_2\text{S}_2$  accumulate on its surface due to the shuttle effect of soluble

polysulfides. Therefore, the stabilization of lithium anodes is of great significance for the application of LSBs.

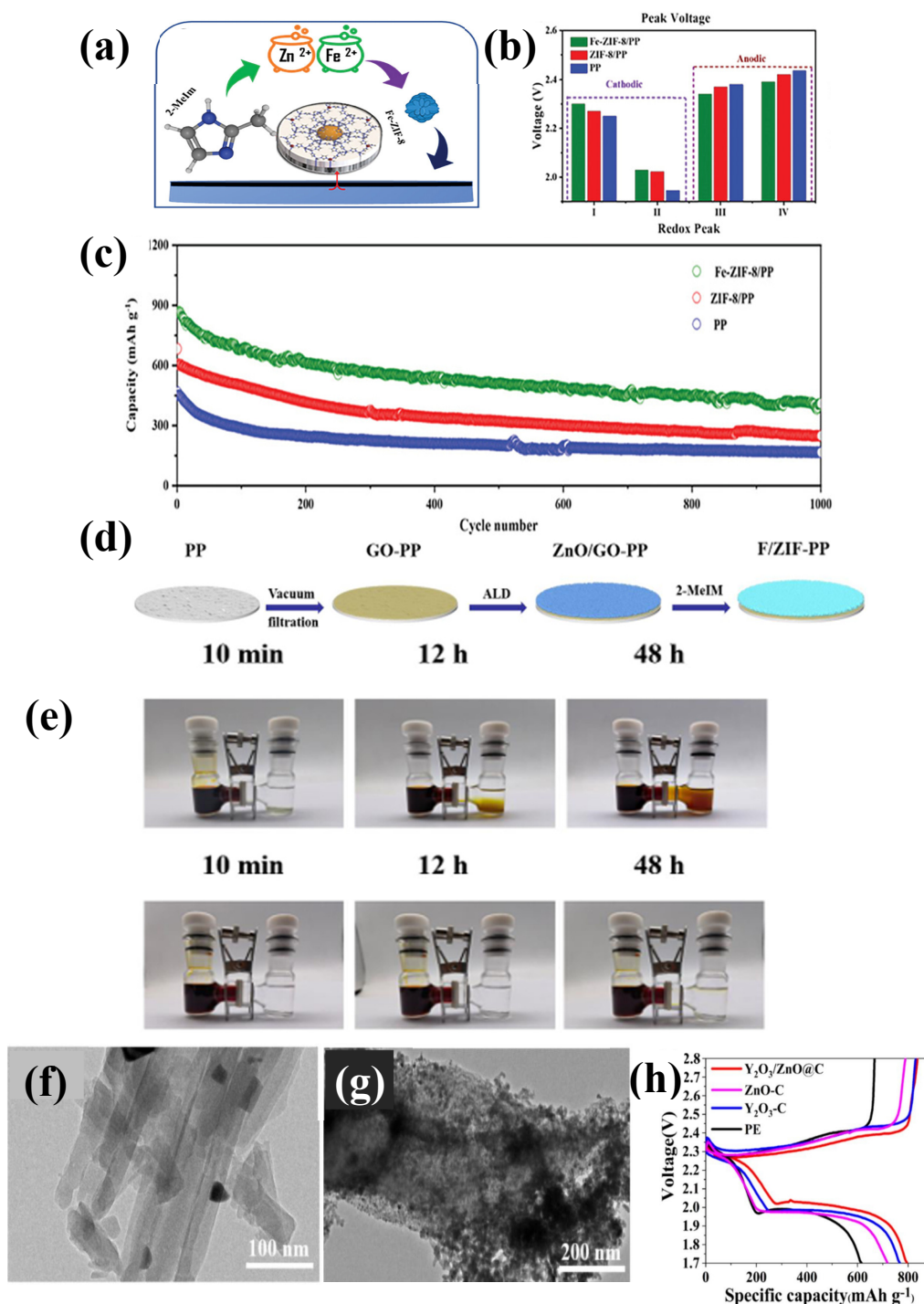


**Figure 11.** (a) Schematic preparation of Fe-ZIF-8. (b) Peak voltage. (c) Energy storage properties of LSBs with different diaphragms. Long-term cycling performance of LSBs at 0.5 C (reprinted/adapted with permission from [79]; copyright 2024, *Advanced Energy Materials*). (d) Schematic preparation of F/ZIF-PP separator. (e) Use of a double L device for the (upper) G-PP and (lower) F/ZIF-PP separators (reprinted/adapted with permission from [80]; copyright 2024, *Interdisciplinary Materials*). (f) ZnO@C TEM image. (g) TEM image of Y<sub>2</sub>O<sub>3</sub>-ZnO@C. (h) Charge–discharge curve at 0.5 C (reprinted/adapted with permission from [87]; copyright 2024, *Journal of Energy Storage*).

Based on such problems, Han et al. [90] used a novel gel polymer electrolyte (GPE) with immobilized anions, which allowed the PVDF-based GPE to be modified and fabricated as

a semi-solid electrolyte by vacuum filtration method using Mg-MOF-74 material. From Figure 12a, it can be seen that the modified GPE can immobilize not only large-sized polysulfide anions but also TFSI-anions, thus promoting uniform lithium-ion flux and homogeneous lithium deposition. Figure 12b shows the ionic conductivity of the three electrolytes; the ionic conductivity of Celgard electrolyte stays at the lowest value of  $3.43 \times 10^{-4} \text{ S cm}^{-1}$ , whereas the ionic conductivity of PVDF electrolyte and MOF-PVDF electrolyte are relatively large at  $4.26 \times 10^{-4}$  and  $6.72 \times 10^{-4} \text{ S cm}^{-1}$ , respectively. While the resistance value of the MOF-modified PVDF electrolyte was marginally higher than that of the pristine PVDF electrolyte, the performance of MOF-modified GPE for LSBs could be seen to be improved due to the increase in thickness and the corresponding ionic conductivity after MOF modification. Different from the above, the all-solid-state electrolyte is compatible with higher specific capacity positive and negative electrode materials, and the solid-state electrolyte has a certain mechanical strength, which can better inhibit the growth of lithium dendrites and resist external stress impact.

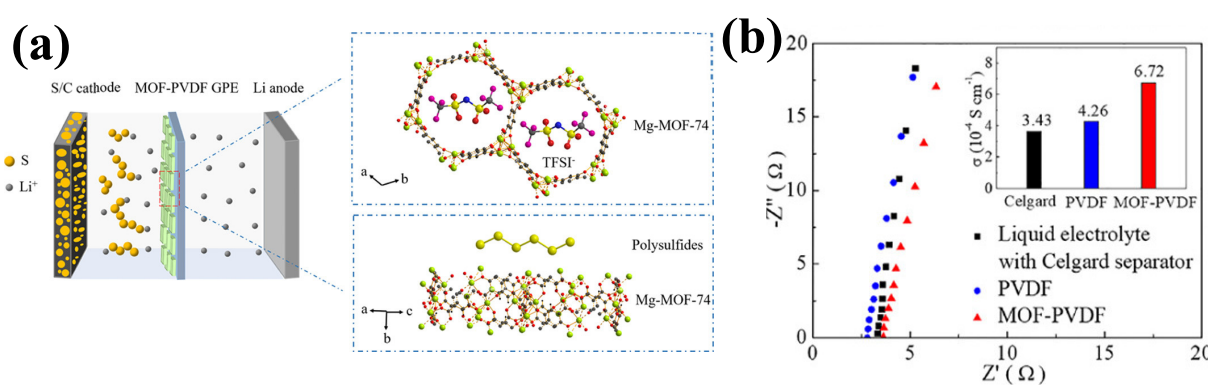


**Figure 12.** (a) Schematic of MOF-PVDF GPE with LSBs' immobilized anions. (b) Impedance spectra and associated ionic conductivities at room temperature for cells with various electrolytes (reprinted/adapted with permission from [90]; copyright 2019, *Applied Materials*).

Li et al. [91] proposed a strategy to prepare MOF-related composite solid-state electrolytes (CSEs) for all-solid-state lithium–sulfur batteries (ASSLSBs) using ordered MOFs as fillers. As a conceptual demonstration, MIL-125-NH<sub>2</sub> (termed 3D MPPLCSE) was successfully prepared by electrospinning and calendering methods with an ordered distribution in a PEO-based electrolyte. An increase in the presence of free TFSI ions on the electrolyte surface of 3D MPPL CSE compared to MPL CSE and PL CSE was shown by Raman results. This suggests that, due to the unique ordered-MOF structure, 3D MPPL CSE can effectively immobilize anions and dissociate LiTFSI through open Ti sites, thereby increasing lithium concentration and potentially enhancing the ionic conductivity of the electrolyte. The decomposition of PL CSE commenced at 350 °C, whereas both MPL CSE and 3D MPPL CSE exhibited lower decomposition temperatures, specifically, 336 °C and 327 °C, respectively. This suggests a greater abundance of amorphous PEO regions within the 3D MPPL CSE and MPL CSE compared to PL CSE. Furthermore, experimental observations revealed that under thermal shock conditions (200 °C for 0.5 h), both MPL CSEs and PL CSEs underwent melting. In contrast, the size and morphology of 3D MPPL CSEs remained largely unchanged. These findings indicate that the ordered arrangement of MIL-125-NH<sub>2</sub> within the 3D MPPL CSE effectively inhibits the crystallization of PEO molecular chains. This structured alignment not only stabilizes the material against thermal stress but also facilitates lithium-ion conduction along the surface of the filler particles, ultimately enhancing the ionic conductivity of the composite.

#### 4. Conclusions and Outlook

This article delves into the versatile applications of MOFs in LSBs, encompassing crucial components like anode carriers, separators, and electrolytes. A comparison of the performance of MOF in lithium–sulfur batteries is summarized in Table 1. It offers in-depth insights into how MOFs function within different parts of LSBs and analyzes the pivotal factors influencing their performance, such as their capacity to adsorb polysulfides and their role in promoting uniform ion deposition. Despite the substantial advancements in the application of MOFs in the LSBs field over the past decade, practical implementation and commercialization still pose challenges, and several core mechanisms remain inadequately explored. The key factors and potential avenues for development are outlined as follows.

**Table 1.** Comparison of MOF performance in batteries.

Composites	Initial Discharge Capacity (mAh g <sup>-1</sup> ) (Current Density)	Terminal Discharge Capacity (mAh g <sup>-1</sup> ) (Cycle Number)	Capacity Retention Rate	Loading Amount of Sulfur	Reference
S@FMNCN-800	1645 (0.1 C)	1220 (200)	74.16%	26.0%	[44]
S@FMNCN-900	1588 (0.1 C)	1024 (200)	64.49%	44.6%	[44]
S@FMNCN-1000	1477 (0.1 C)	669 (200)	45.3%	40.3%	[44]
In-IPA@rGO/S	1672.3 (0.2 C)	898.7 (100)	53.74%	25%	[49]
In-IPA/S	1099.4 (0.2 C)	296.7 (100)	26.99%	/	[49]
CoMoS3.13@NCNTs	960 (0.5 C)	586 (1000)	61.04%	72%	[55]
CoMoS3.13	888 (0.5 C)	296 (1000)	33.33%	/	[55]
S/NiCo-PCNF	1431.7 (0.2 C)	628.5 (500)	43.9%	53.5%	[67]
S/Ni-PCNF	1043.2 (0.2 C)	/	/	/	[67]
S/Co-PCNF	988.7 (0.2 C)	/	/	/	[67]
S/PCNF	836.7 (0.2 C)	/	/	/	[67]
Fe-ZIF-8/PP	865 (0.5 C)	409 (1000)	47.28%	/	[77]
ZIF-8/PP	683 (0.5 C)	249 (1000)	36.46%	/	[77]
PP	466 (0.5 C)	167 (1000)	35.84%	/	[77]

- When assessing the impact of MOFs on the performance of LSBs, a comprehensive analysis of the pore structure of MOFs is essential. While most studies have emphasized the role of pore size in mitigating the polysulfide shuttle effect, they often overlook the broader implications of pore size on the uniform distribution of sulfur and the sulfur loading capacity within MOFs. Notably, achieving uniform sulfur loading and increasing sulfur content remain significant challenges for many MOFs. Therefore, these factors must be comprehensively considered during the screening and design of MOFs with optimal pore sizes.
- Applying a uniform and comprehensive MOF coating onto the separator can significantly enhance the interfacial stability and cycling performance of the battery. This coating serves as an effective physical barrier to minimize the polysulfide shuttle effect, while simultaneously providing chemical adsorption sites to improve polysulfide immobilization. Current modification methods, such as vacuum filtration and in situ modification, fall short in meeting this requirement. Therefore, innovative techniques must be adopted for depositing MOF coatings. Promising approaches include chemical vapor deposition, magnetron sputtering, and atomic layer deposition.
- The development of novel redox-active MOFs presents a promising avenue, as these materials not only possess ultra-high specific surface areas and substantial porosity but also offer customizable host–guest interaction platforms. Among these, MOFs

based on tetravalent metals and carboxylic acid ligands have garnered particular attention due to their exceptional chemical stability.

4. The industrial-scale production of metal–organic framework (MOF) materials holds the potential to vastly expand their applicability in commercial lithium–sulfur batteries (LSBs). To achieve cost reduction, it is crucial to select earth-abundant raw materials and employ synthesis methods that yield high productivity with minimal by-products. Emerging synthesis strategies, such as solid–solid and gas-phase methods, which feature shorter production cycles and higher yields, will play a key role in advancing the industrial manufacturing of MOF materials.

Despite numerous challenges, the application of MOFs in the field of LSBs has advanced rapidly, offering a clear pathway for the development of MOF-based materials for next-generation LSBs. Future research endeavors will focus on identifying cost-effective MOF materials suitable for large-scale industrial deployment, as well as pushing forward the progress of commercial LSBs with high energy density and exceptional cycling stability. This comprehensive summary and forward-looking perspective will serve as a crucial scientific foundation for the development of novel MOF-based cathode materials, the large-scale production of functional separators incorporating MOFs, and the strategic design of innovative MOF-based electrolytes.

**Author Contributions:** Investigation, Q.Z. and W.S.; writing—original draft preparation, Q.Z. and W.S.; writing—review and editing, H.Z.; supervision, D.M.; funding acquisition, Q.Z. All authors have read and agreed to the published version of the manuscript.

**Funding:** This research was funded by the National Natural Science Foundation of China (22105047) and the Guangxi Natural Science Foundation (2021GXNSFBA196029).

**Acknowledgments:** We acknowledge the support from the Guangxi University of Science and Technology Doctoral Fund (19Z10).

**Conflicts of Interest:** The authors declare no conflicts of interest.

## References

1. Guo, J.; Meng, X.; Wang, Q.; Zhang, Y.; Yan, S.; Luo, S. Advancements in Lithium–Oxygen Batteries: A Comprehensive Review of Cathode and Anode Materials. *Batteries* **2024**, *10*, 260. [[CrossRef](#)]
2. Hou, S.E.; Alonso, J.A.; Rajasekharan, S.; Martínez-Lope, M.J.; Fernández-Díaz, M.T.; Goodenough, J.B. Defective Ni Perovskites as Cathode Materials in Intermediate-Temperature Solid-Oxide Fuel Cells: A Structure-Properties Correlation. *Chem. Mater.* **2010**, *22*, 1071–1079. [[CrossRef](#)]
3. Ting, M.; Yue, H.X.; Xiao, Y.B.; Huang, Y.X.; Li, X.; Gao, X.; He, N.; Zhan, C.Z.; Ding, N. A review of organic sulfur applications in lithium-sulfur batteries. *J. Power Sources* **2024**, *625*, 717.
4. Lv, Z.-C.; Wang, P.-F.; Wang, J.-C.; Tian, S.-H.; Yi, T.-F. Key challenges, recent advances and future perspectives of rechargeable lithium-sulfur batteries. *J. Ind. Eng. Chem.* **2023**, *124*, 68–88. [[CrossRef](#)]
5. Miao, Y.; Zheng, Y.; Tao, F.; Chen, Z.; Xiong, Y.; Ren, F.; Liu, Y. Synthesis and application of single-atom catalysts in sulfur cathode for high-performance lithium–sulfur batteries. *Chin. Chem. Lett.* **2023**, *34*, 107121. [[CrossRef](#)]
6. Chavan, V.D.; Patil, P.D.; Patil, C.S.; Patil, S.R.; Katkar, P.K.; Sheikh, Z.A.; Ustad, R.E.; Kim, H.; Kadam, K.D.; Patil, H.S.; et al. Advanced functional materials and their coordinated composites for next-generation Li-S batteries: A brief review. *J. Energy Storage* **2024**, *88*, 111572. [[CrossRef](#)]
7. Liu, J.; Wang, F.; Wei, H.; Liu, Y.; Zhai, X.; Wen, S.; Zhang, Q. Fabrication and application of binder-free cathodes in high-performance lithium-chalcogen (S, Se, Te) batteries: A review. *Chin. Chem. Lett.* **2024**, *110475*. [[CrossRef](#)]
8. Li, Z.; He, Q.; Xu, X.; Zhao, Y.; Liu, X.; Zhou, C.; Ai, D.; Xia, L.; Mai, L. A 3D Nitrogen-Doped Graphene/TiN Nanowires Composite as a Strong Polysulfide Anchor for Lithium–Sulfur Batteries with Enhanced Rate Performance and High Areal Capacity. *Adv. Mater.* **2018**, *30*, 1804089. [[CrossRef](#)] [[PubMed](#)]
9. Mei, J.; Liao, T.; Liang, J.; Qiao, Y.; Dou, S.X.; Sun, Z. Toward Promising Cathode Catalysts for Nonlithium Metal–Oxygen Batteries. *Adv. Energy Mater.* **2019**, *10*, 1901997. [[CrossRef](#)]

10. Phung, J.; Zhang, X.; Deng, W.; Li, G. An overview of MOF-based separators for lithium-sulfur batteries. *Sustain. Mater. Technol.* **2022**, *31*, e00374. [[CrossRef](#)]
11. Yuan, N.; Sun, W.; Yang, J.; Gong, X.; Liu, R. Multifunctional MOF-Based Separator Materials for Advanced Lithium–Sulfur Batteries. *Adv. Mater.* **2021**, *8*, 2001941. [[CrossRef](#)]
12. Ajdari, F.B.; Shahrak, M.N.; Ershadi, M.; Shakourian-Fard, M.; Abbasi, F.; Kamath, G.; Beni, F.A.; Ghasemi, F.; Ghenaatian, H.R.; Ramakrishna, S. Lithium–sulfur batteries beyond lithium-ion counterparts: Reasonable substituting challenges, current research focus, binding critical role, and cathode designing. *Rev. Chem. Eng.* **2024**, *40*, 973–1022. [[CrossRef](#)]
13. Zhou, X.; Wang, Y.; Gu, Y.; Su, J.; Liu, Y.; Yin, Y.; Yuan, S.; Ma, J.; Jin, Z.; Zuo, J.-L. All-purpose redox-active metal-organic frameworks as both cathodic and anodic host materials for advanced lithium-sulfur batteries. *Matter* **2024**, *7*, 3069–3082. [[CrossRef](#)]
14. Zhang, J.; Jiang, G.; Cumberland, T.; Xu, P.; Wu, Y.; Delaat, S.; Yu, A.; Chen, Z. A highly sensitive breathable fuel cell gas sensor with nanocomposite solid electrolyte. *InfoMat* **2019**, *1*, 234–241. [[CrossRef](#)]
15. Wang, Y.; Li, B.; Zhang, B.; Tian, S.; Yang, X.; Ye, H.; Xia, Z.; Zheng, G. Application of MOFs-derived mixed metal oxides in energy storage. *J. Electroanal. Chem.* **2020**, *878*, 114576. [[CrossRef](#)]
16. Ran, F.; Xu, X.; Pan, D.; Liu, Y.; Bai, Y.; Shao, L. Ultrathin 2D Metal–Organic Framework Nanosheets In situ Interpenetrated by Functional CNTs for Hybrid Energy Storage Device. *Nano-Micro Lett.* **2020**, *12*, 46. [[CrossRef](#)]
17. Zhang, K.; Zhang, Y.; Zhang, Q.; Liang, Z.; Gu, L.; Guo, W.; Zhu, B.; Guo, S.; Zou, R. Metal-organic framework-derived Fe/Cu-substituted Co nanoparticles embedded in CNTs-grafted carbon polyhedron for Zn-air batteries. *Carbon Energy* **2020**, *2*, 283–293. [[CrossRef](#)]
18. Xia, J.; Xu, P.; Wang, W.; Hu, P.; Sun, Y.; Shao, J. Carbon Nanofiber-Based Sandwich Free-Standing Cathode for High-Performance Lithium–Sulfur Batteries. *Langmuir* **2024**, *40*, 15688–15699. [[CrossRef](#)]
19. Theibault, M.J.; McCormick, C.R.; Lang, S.; Schaak, R.E.; Abruna, H.D. High Entropy Sulfide Nanoparticles as Lithium Polysulfide Redox Catalysts. *ACS Nano* **2023**, *17*, 18402–18410. [[CrossRef](#)]
20. Zhang, J.; Ma, W.; Feng, Z.; Wu, F.; Wei, D.; Xi, B.; Xiong, S. P-doped BN nanosheets decorated graphene as the functional interlayer for Li–S batteries. *J. Energy Chem.* **2019**, *39*, 54–60. [[CrossRef](#)]
21. Zhu, X.; Wang, L.; Bai, Z.; Lu, J.; Wu, T. Sulfide-Based All-Solid-State Lithium–Sulfur Batteries: Challenges and Perspectives. *Nano-Micro Lett.* **2023**, *15*, 75. [[CrossRef](#)] [[PubMed](#)]
22. Lim, W.G.; Kim, S.; Jo, C.; Lee, J. A Comprehensive Review of Materials with Catalytic Effects in Li–S Batteries: Enhanced Redox Kinetics. *Angew. Chem. Int. Ed.* **2019**, *58*, 18746–18757. [[CrossRef](#)]
23. Zak, J.J.; Kim, S.S.; Laskowski, F.A.L.; See, K.A. An Exploration of Sulfur Redox in Lithium Battery Cathodes. *J. Am. Chem. Soc.* **2022**, *144*, 10119–10132. [[CrossRef](#)]
24. Zhang, M.; Chen, W.; Xue, L.; Jiao, Y.; Lei, T.; Chu, J.; Huang, J.; Gong, C.; Yan, C.; Yan, Y.; et al. Adsorption-Catalysis Design in the Lithium–Sulfur Battery. *Adv. Energy Mater.* **2020**, *10*, 1903008. [[CrossRef](#)]
25. Zhou, G.M.; Chen, H.; Cui, Y. Formulating energy density for designing practical lithium–sulfur batteries. *Nat. Energy* **2022**, *7*, 312–319. [[CrossRef](#)]
26. Qi, F.; Sun, Z.; Fan, X.; Wang, Z.; Shi, Y.; Hu, G.; Li, F. Tunable Interaction between Metal-Organic Frameworks and Electroactive Components in Lithium–Sulfur Batteries: Status and Perspectives. *Adv. Energy Mater.* **2021**, *11*, 2100387. [[CrossRef](#)]
27. Zhang, Y.; Zhang, X.; Silva, S.R.P.; Ding, B.; Zhang, P.; Shao, G. Lithium–Sulfur Batteries Meet Electrospinning: Recent Advances and the Key Parameters for High Gravimetric and Volume Energy Density. *Adv. Sci.* **2021**, *9*, 2103879. [[CrossRef](#)]
28. Zhao, F.L.; Xue, J.H.; Shao, W.; Yu, H.; Huang, W.; Xiao, J. Toward high-sulfur-content, high-performance lithium-sulfur batteries: Review of materials and technologies. *J. Energy Chem.* **2023**, *80*, 625–657. [[CrossRef](#)]
29. Lu, J.; Luo, S.; Qi, Z.; Chen, T.; Li, X.; Yuan, T.; Pang, Y.; Zheng, S. Recent advances in transition metal chalcogenide derivatives from metal-organic frameworks for lithium-sulfur batteries. *Cell Rep. Phys. Sci.* **2024**, *5*, 102028. [[CrossRef](#)]
30. Chen, Z.X.; Zhao, M.; Hou, L.P.; Zhang, X.Q.; Li, B.Q.; Huang, J.Q. Toward Practical High-Energy-Density Lithium-Sulfur Pouch Cells: A Review. *Adv. Mater.* **2022**, *34*, 2201555. [[CrossRef](#)] [[PubMed](#)]
31. Feng, S.; Fu, Z.H.; Chen, X.; Zhang, Q. A review on theoretical models for lithium-sulfur battery cathodes. *InfoMat* **2022**, *4*, e12304. [[CrossRef](#)]
32. Hussain, I.; Zhang, K. MOF-derived scaffolds as electrode materials: A mini-review. *Nanoscale* **2024**, *16*, 15515–15528. [[CrossRef](#)] [[PubMed](#)]
33. Hwang, J. A review of synthesis strategies for MOF-derived single atom catalysts. *Korean J. Chem. Eng.* **2021**, *38*, 1104–1116. [[CrossRef](#)]
34. Li, X.; Yang, X.; Xue, H.; Pang, H.; Xu, Q. Metal–organic frameworks as a platform for clean energy applications. *EnergyChem* **2020**, *2*, 100027. [[CrossRef](#)]
35. Lu, C.; Clayville, B.; Choi, J.Y.; Park, J. 2D metal-organic frameworks as an emerging platform with tunable electronic structures. *Chem* **2023**, *9*, 2757–2770. [[CrossRef](#)]

36. Xuan, W.; Zhu, C.; Liu, Y.; Cui, Y. Mesoporous metal–organic framework materials. *Chem. Soc. Rev.* **2011**, *41*, 1677–1695. [CrossRef] [PubMed]
37. Islamoglu, T.; Goswami, S.; Li, Z.; Howarth, A.J.; Farha, O.K.; Hupp, J.T. Correction to Postsynthetic Tuning of Metal–Organic Frameworks for Targeted Applications. *Acc. Chem. Res.* **2018**, *51*, 212. [CrossRef] [PubMed]
38. Lee, J.; Choi, I.; Kim, E.; Park, J.; Nam, K.W. Metal-organic frameworks for high-performance cathodes in batteries. *iScience* **2024**, *27*, 110211. [CrossRef]
39. Yang, S.; Karve, V.V.; Justin, A.; Kochetygov, I.; Espín, J.; Asgari, M.; Trukhina, O.; Sun, D.T.; Peng, L.; Queen, W.L. Enhancing MOF performance through the introduction of polymer guests. *Coord. Chem. Rev.* **2021**, *427*, 213525. [CrossRef]
40. Nadar, S.S.; Vaidya, L.; Rathod, V.K. Enzyme embedded metal organic framework (enzyme-MOF): De novo approaches for immobilization. *Int. J. Biol. Macromol.* **2020**, *149*, 861–876. [CrossRef]
41. Li, Z.; Guo, Y.; Li, K.; Wang, S.; De Bonis, E.; Cao, H.; Mertens, S.F.L.; Teng, C. Shape control of bimetallic MOF/Graphene composites for efficient oxygen evolution reaction. *J. Electroanal. Chem.* **2023**, *930*, 117144. [CrossRef]
42. Ma, Y.; Wu, M.; Li, L.; Li, Z.; Zhao, X.; Lian, R.; Zhang, W. MOF derived Co9S8 nanoparticles embedded in 3D N-doped carbon matrix for high-performance K-ion battery anode. *Appl. Surf. Sci.* **2022**, *600*, 154159. [CrossRef]
43. Demir-Cakan, R.; Morcrette, M.; Nouar, F.; Davoisne, C.; Devic, T.; Gonbeau, D.; Dominko, R.; Serre, C.; Férey, G.; Tarascon, J.-M. Cathode Composites for Li–S Batteries via the Use of Oxygenated Porous Architectures. *J. Am. Chem. Soc.* **2011**, *133*, 16154–16160. [CrossRef] [PubMed]
44. Hong, X.-J.; Tang, X.-Y.; Wei, Q.; Song, C.-L.; Wang, S.-Y.; Dong, R.-F.; Cai, Y.-P.; Si, L.-P. Efficient Encapsulation of Small S<sub>2</sub>-4 Molecules in MOF-Derived Flowerlike Nitrogen-Doped Microporous Carbon Nanosheets for High-Performance Li–S Batteries. *ACS Appl. Mater. Interfaces* **2018**, *10*, 9435–9443. [CrossRef] [PubMed]
45. Jeon, Y.; Lee, J.; Jo, H.; Hong, H.; Lee, L.Y.S.; Piao, Y. Co/Co<sub>3</sub>O<sub>4</sub>-embedded N-doped hollow carbon composite derived from a bimetallic MOF/ZnO Core-shell template as a sulfur host for Li–S batteries. *Chem. Eng. J.* **2021**, *407*, 126967. [CrossRef]
46. Park, M.-S.; Yu, J.-S.; Kim, K.J.; Jeong, G.; Kim, J.-H.; Jo, Y.-N.; Hwang, U.; Kang, S.; Woo, T.; Kim, Y.-J. One-step synthesis of a sulfur-impregnated graphene cathode for lithium–sulfur batteries†. *Phys. Chem. Chem. Phys.* **2012**, *14*, 6796–6804. [CrossRef] [PubMed]
47. Zhang, M.; Shan, Y.; Kong, Q.; Pang, H. Applications of metal–organic framework–graphene composite materials in electrochemical energy storage. *FlatChem* **2022**, *32*, 100332. [CrossRef]
48. Baumann, A.E.; Downing, J.R.; Burns, D.A.; Hersam, M.C.; Thoi, V.S. Graphene–Metal–Organic Framework Composite Sulfur Electrodes for Li–S Batteries with High Volumetric Capacity. *ACS Appl. Mater. Interfaces* **2020**, *12*, 37173–37181. [CrossRef] [PubMed]
49. Jiao, X.; Deng, T.; Men, X.; Zuo, Y.; Wang, J. Indium metal-organic framework with catalytic sites coated conductive graphene for high-performance lithium-sulfur batteries. *Ceram. Int.* **2022**, *48*, 16754–16763. [CrossRef]
50. Qian, X.; Cheng, J.; Wang, Y.; Jin, L.; Chen, J.; Hao, Q.; Zhang, K. A Ni-MOF derived graphene oxide combined Ni<sub>3</sub>S<sub>2</sub>–Ni/C composite and its use in the separator coating for lithium sulfur batteries. *Phys. Chem. Chem. Phys.* **2023**, *25*, 5559–5568. [CrossRef] [PubMed]
51. Zuluaga-Gómez, C.C.; Plaza-Rivera, C.O.; Tripathi, B.; Katiyar, R.K.; Pradhan, D.K.; Morell, G.; Lin, Y.; Correa, M.; Katiyar, R.S. Holey Graphene/Ferroelectric/Sulfur Composite Cathodes for High-Capacity Lithium–Sulfur Batteries. *ACS Omega* **2023**, *8*, 13097–13108. [CrossRef]
52. Xu, G.; Zuo, Y.; Huang, B. Metal-organic framework-74-Ni/carbon nanotube composite as sulfur host for high performance lithium-sulfur batteries. *J. Electroanal. Chem.* **2018**, *830*, 43–49. [CrossRef]
53. Zhou, F.; Qiao, Z.; Zhang, Y.; Xu, W.; Zheng, H.; Xie, Q.; Luo, Q.; Wang, L.; Qu, B.; Peng, D.-L. Bimetallic MOF-derived CNTs-grafted carbon nanocages as sulfur host for high-performance lithium–sulfur batteries. *Electrochim. Acta* **2020**, *349*, 136378. [CrossRef]
54. Li, Z.; Wu, H.B.; Lou, X.W. Rational designs and engineering of hollow micro-/nanostructures as sulfur hosts for advanced lithium–sulfur batteries. *Energy Environ. Sci.* **2016**, *9*, 3061–3070. [CrossRef]
55. Wang, J.; Chen, X.; Chen, L.; Jiang, A.; Zeng, Y.; Li, X.; Xiao, J. Layered CoMoS<sub>3</sub>.13@NCNTs with a Rod-Shaped Skeleton as the Cathode of Lithium–Sulfur Batteries. *ACS Sustain. Chem. Eng.* **2024**, *12*, 9864–9873. [CrossRef]
56. Niščáková, V.; Gubová, A.; Petruš, O.; Fei, H.; Almáši, M.; Fedorková, A.S. Investigation of polypyrrole based composite material for lithium sulfur batteries. *Sci. Rep.* **2024**, *14*, 22928. [CrossRef]
57. Yang, J.; Li, S.; Wu, G.; Bao, J.; Xu, S.; Gu, C.; Lv, J.; Huang, J.; Joo, S.W. Preparation of polyaniline-coated cobalt nitride nanoflowers as sulfur host for advanced lithium–sulfur battery. *J. Alloys Compd.* **2024**, *981*, 173701. [CrossRef]
58. Wei, W.; Li, J.; Wang, Q.; Liu, D.; Niu, J.; Liu, P. Hierarchically Porous SnO<sub>2</sub> Nanoparticle-Anchored Polypyrrole Nanotubes as a High-Efficient Sulfur/Polysulfide Trap for High-Performance Lithium–Sulfur Batteries. *ACS Appl. Mater. Interfaces* **2020**, *12*, 6362–6370. [CrossRef] [PubMed]

59. Liu, P.-Y.; Zhao, J.-J.; Dong, Z.-P.; Liu, Z.-L.; Wang, Y.-Q. Interwoving polyaniline and a metal-organic framework grown in situ for enhanced supercapacitor behavior. *J. Alloys Compd.* **2021**, *854*, 157181. [[CrossRef](#)]
60. Zhang, H.; Feng, S.; Li, X.; Chen, X.; Chen, L.; Xiao, J. Porous structure of fixed sulfur and networked electronic channels in three-dimensional skeletal structure of polyaniline and MOF-derived materials. *Colloids Surf. A Physicochem. Eng. Asp.* **2023**, *669*, 131440. [[CrossRef](#)]
61. Li, B.; Xie, M.; Yi, G.; Zhang, C. Biomass-derived activated carbon/sulfur composites as cathode electrodes for Li–S batteries by reducing the oxygen content. *RSC Adv.* **2020**, *10*, 2823–2829. [[CrossRef](#)] [[PubMed](#)]
62. Sun, Z.; Sun, B.; Xue, J.; He, J.; Zhao, R.; Chen, Z.; Sun, Z.; Liu, H.; Dou, S. ZIF-67/ZIF-8 and its Derivatives for Lithium Sulfur Batteries. *Adv. Funct. Mater.* **2024**, *35*, 2414671. [[CrossRef](#)]
63. Liu, Y.; Dong, S.; Wang, L.; Chen, G.; Hou, Y.; Cao, Z.; Zhang, Y. Bimetal cobalt-zinc MOF and its derivatives as anode materials for lithium-ion batteries. *J. Solid State Electrochem.* **2022**, *26*, 2301–2313. [[CrossRef](#)]
64. Kyom Kim, D.; Seul Byun, J.; Moon, S.; Choi, J.; Ha Chang, J.; Suk, J. Molten salts approach of metal-organic framework-derived nitrogen-doped porous carbon as sulfur host for lithium-sulfur batteries. *Chem. Eng. J.* **2022**, *441*, 135945. [[CrossRef](#)]
65. Bai, Y.; Jiao, X.; Chen, L.; Huang, L.; Xue, K.; Wu, D.; Li, X.; Li, Y.; Deng, T.; Wang, J. Regulating In-MOF derivatives for bidirectionally boosting redox kinetics of sulfur cathodes. *Ceram. Int.* **2024**, *50*, 8370–8377. [[CrossRef](#)]
66. Dong, C.; Zhou, C.; Wu, M.; Yu, Y.; Yu, K.; Yan, K.; Shen, C.; Gu, J.; Yan, M.; Sun, C.; et al. Boosting Bi-Directional Redox of Sulfur with Dual Metal Single Atom Pairs in Carbon Spheres Toward High-Rate and Long-Cycling Lithium–Sulfur Battery. *Adv. Energy Mater.* **2023**, *13*, 2301505. [[CrossRef](#)]
67. Wang, Z.; Liu, C.; Wang, Y.; Zhang, S.; Huang, M.; Bai, J.; Wang, H.; Liu, X. Nitrogen-doped carbon nanofiber loaded MOF-derived NiCo bimetallic nanoparticles accelerate the redox transformation of polysulfide for lithium–sulfur batteries. *J. Electroanal. Chem.* **2024**, *959*, 118185. [[CrossRef](#)]
68. Guan, J.; Feng, X.; Zeng, Q.; Li, Z.; Liu, Y.; Chen, A.; Wang, H.; Cui, W.; Liu, W.; Zhang, L. A New In Situ Prepared MOF-Natural Polymer Composite Electrolyte for Solid Lithium Metal Batteries with Superior High- Rate Capability and Long-Term Cycling Stability at Ultrahigh Current Density. *Adv. Sci.* **2022**, *10*, 2203916. [[CrossRef](#)] [[PubMed](#)]
69. Luo, S.; Deng, N.; Wang, H.; Zeng, Q.; Li, Y.; Kang, W.; Cheng, B. Facilitating Li<sup>+</sup> conduction channels and suppressing lithium dendrites by introducing Zn-based MOFs in composite electrolyte membrane with excellent thermal stability for solid-state lithium metal batteries. *Chem. Eng. J.* **2023**, *474*, 145683. [[CrossRef](#)]
70. Wang, Q.; Cui, K.-P.; Liu, T.; Li, C.-X.; Liu, J.; Kong, D.-C.; Weerasooriya, R.; Chen, X. In situ growth of NH<sub>2</sub>-MIL-101 metal organic frameworks on biochar for glyphosate adsorption. *Chemosphere* **2023**, *331*, 138827. [[CrossRef](#)]
71. Raza, H.; Cheng, J.; Lin, C.; Majumder, S.; Zheng, G.; Chen, G. High-entropy stabilized oxides derived via a low-temperature template route for high-performance lithium-sulfur batteries. *EcoMat* **2023**, *5*, e12324. [[CrossRef](#)]
72. Raza, H.; Cheng, J.; Wang, J.; Kandasamy, S.; Zheng, G.; Chen, G. Titanium-containing high entropy oxide (Ti-HEO): A redox expediting electrocatalyst towards lithium polysulfides for high performance Li-S batteries. *Nano Res. Energy* **2024**, *3*, e9120116. [[CrossRef](#)]
73. Zhou, C.; Li, Z.; Xu, X.; Mai, L. Metal-organic frameworks enable broad strategies for lithium-sulfur batteries. *Natl. Sci. Rev.* **2021**, *8*, nwab055. [[CrossRef](#)] [[PubMed](#)]
74. Zhou, L.; Danilov, D.L.; Eichel, R.A.; Notten, P.H.L. Host Materials Anchoring Polysulfides in Li–S Batteries Reviewed. *Adv. Energy Mater.* **2020**, *11*, 2001304. [[CrossRef](#)]
75. Chen, Y.; Wang, T.; Tian, H.; Su, D.; Zhang, Q.; Wang, G. Advances in Lithium–Sulfur Batteries: From Academic Research to Commercial Viability. *Adv. Mater.* **2021**, *33*, 2003666. [[CrossRef](#)] [[PubMed](#)]
76. Zhang, T.; Zhang, L.; Hou, Y. MXenes: Synthesis strategies and lithium-sulfur battery applications. *eScience* **2022**, *2*, 164–182. [[CrossRef](#)]
77. Yang, Y.; Ma, S.; Xia, M.; Guo, Y.; Zhang, Y.; Liu, L.; Zhou, C.; Chen, G.; Wang, X.; Wu, Q.; et al. Elaborately converting hierarchical NiCo–LDH to rod-like LDH-decorated MOF as interlayer for high–performance lithium–sulfur battery. *Mater. Today Phys.* **2023**, *35*, 101112. [[CrossRef](#)]
78. Kang, H.; Shin, J.; Kim, T.-H.; Lee, Y.; Lee, D.; Lee, J.; Kim, G.; Cho, E. Metal–Organic Framework-Derived Magnesium Oxide@Carbon Interlayer for Stable Lithium–Sulfur Batteries. *ACS Sustain. Chem. Eng.* **2023**, *11*, 1344–1354. [[CrossRef](#)]
79. Razaq, R.; Din, M.M.U.; Småbråten, D.R.; Eyupoglu, V.; Janakiram, S.; Sunde, T.O.; Allahgoli, N.; Rettenwander, D.; Deng, L. Synergistic Effect of Bimetallic MOF Modified Separator for Long Cycle Life Lithium-Sulfur Batteries. *Adv. Energy Mater.* **2023**, *14*, 2302897. [[CrossRef](#)]
80. Zhou, C.; Dong, C.; Wang, W.; Tian, Y.; Shen, C.; Yan, K.; Mai, L.; Xu, X. An ultrathin and crack-free metal-organic framework film for effective polysulfide inhibition in lithium–sulfur batteries. *Interdiscip. Mater.* **2024**, *3*, 306–315. [[CrossRef](#)]
81. Li, C.; Liu, R.; Xiao, Y.; Cao, F.; Zhang, H. Recent progress of separators in lithium-sulfur batteries. *Energy Storage Mater.* **2021**, *40*, 439–460. [[CrossRef](#)]

82. Luo, Z.; Wu, Y.; Xu, X.; Ju, W.; Lei, W.; Wu, D.; Pan, J.; Ouyang, X. Surface-coated AlF<sub>3</sub> nanolayers enable polysulfide confinement within biomass-derived nitrogen-doped hierarchical porous carbon microspheres for improved lithium-sulfur batteries. *J. Colloid Interface Sci.* **2024**, *660*, 657–668. [CrossRef] [PubMed]
83. Wang, T.; He, J.; Zhu, Z.; Cheng, X.-B.; Zhu, J.; Lu, B.; Wu, Y. Heterostructures Regulating Lithium Polysulfides for Advanced Lithium-Sulfur Batteries. *Adv. Mater.* **2023**, *35*, 2303520. [CrossRef] [PubMed]
84. Wang, Y.; Ai, R.; Wang, F.; Hu, X.; Zeng, Y.; Hou, J.; Zhao, J.; Zhang, Y.; Zhang, Y.; Li, X. Research Progress on Multifunctional Modified Separator for Lithium–Sulfur Batteries. *Polymers* **2023**, *15*, 993. [CrossRef]
85. Zhou, J.; Sun, A. Progress in the advancement of atomically dispersed catalysts for enhanced performance lithium-sulfur batteries. *Chem. Eng. J.* **2024**, *488*, 150719. [CrossRef]
86. Zhu, Y.; Chen, Z.; Chen, H.; Fu, X.; Awuye, D.E.; Yin, X.; Zhao, Y. Breaking the Barrier: Strategies for Mitigating Shuttle Effect in Lithium–Sulfur Batteries Using Advanced Separators. *Polymers* **2023**, *15*, 3955. [CrossRef] [PubMed]
87. Zhao, S.; Hao, Q.; Qian, X.; Jin, L.; Li, B.; Xu, H. Application of Y-Zn-MOF derived Y<sub>2</sub>O<sub>3</sub>/ZnO@C in modification of lithium-sulfur battery separator. *J. Energy Storage* **2024**, *101*, 113833. [CrossRef]
88. Liang, Z.; Lin, D.; Zhao, J.; Lu, Z.; Liu, Y.; Liu, C.; Lu, Y.; Wang, H.; Yan, K.; Tao, X.; et al. Composite lithium metal anode by melt infusion of lithium into a 3D conducting scaffold with lithophilic coating. *Proc. Natl. Acad. Sci. USA* **2016**, *113*, 2862–2867. [CrossRef] [PubMed]
89. Zhang, R.; Chen, X.-R.; Chen, X.; Cheng, X.-B.; Zhang, X.-Q.; Yan, C.; Zhang, Q. Lithiophilic Sites in Doped Graphene Guide Uniform Lithium Nucleation for Dendrite-Free Lithium Metal Anodes. *Angew. Chem. Int. Ed.* **2017**, *56*, 7764–7768. [CrossRef] [PubMed]
90. Han, D.-D.; Wang, Z.-Y.; Pan, G.-L.; Gao, X.-P. Metal–Organic-Framework-Based Gel Polymer Electrolyte with Immobilized Anions To Stabilize a Lithium Anode for a Quasi-Solid-State Lithium–Sulfur Battery. *ACS Appl. Mater. Interfaces* **2019**, *11*, 18427–18435. [CrossRef] [PubMed]
91. Li, J.; Xie, F.; Pang, W.; Liang, Q.; Yang, X.; Zhang, L. Regulate transportation of ions and polysulfides in all-solid-state Li-S batteries using ordered-MOF composite solid electrolyte. *Sci. Adv.* **2024**, *10*, eadl3925. [CrossRef]

**Disclaimer/Publisher’s Note:** The statements, opinions and data contained in all publications are solely those of the individual author(s) and contributor(s) and not of MDPI and/or the editor(s). MDPI and/or the editor(s) disclaim responsibility for any injury to people or property resulting from any ideas, methods, instructions or products referred to in the content.